



**HAL**  
open science

# Calcium and copper substitution in stoichiometric and La-deficient LaFeO<sub>3</sub> compositions: A starting point in next generation of Three-Way-Catalysts for gasoline engines

Jianxiong Wu, Jean-Philippe Dacquin, Nora Djelal, Catherine Cordier, Christophe Dujardin, Pascal Granger

## ► To cite this version:

Jianxiong Wu, Jean-Philippe Dacquin, Nora Djelal, Catherine Cordier, Christophe Dujardin, et al.. Calcium and copper substitution in stoichiometric and La-deficient LaFeO<sub>3</sub> compositions: A starting point in next generation of Three-Way-Catalysts for gasoline engines. Applied Catalysis B: Environmental, 2021, Applied Catalysis B: Environmental, 282, pp.119621. 10.1016/j.apcatb.2020.119621 . hal-03213759

**HAL Id: hal-03213759**

**<https://hal.univ-lille.fr/hal-03213759>**

Submitted on 17 Oct 2022

**HAL** is a multi-disciplinary open access archive for the deposit and dissemination of scientific research documents, whether they are published or not. The documents may come from teaching and research institutions in France or abroad, or from public or private research centers.

L'archive ouverte pluridisciplinaire **HAL**, est destinée au dépôt et à la diffusion de documents scientifiques de niveau recherche, publiés ou non, émanant des établissements d'enseignement et de recherche français ou étrangers, des laboratoires publics ou privés.



Distributed under a Creative Commons Attribution - NonCommercial 4.0 International License

Manuscript for submission to the journal Applied Catalysis B  
Manuscript ID: APCATB-D-20-03506R1

# Calcium and copper substitution in stoichiometric and La-deficient LaFeO<sub>3</sub> compositions: A starting point in next generation of Three-Way-Catalysts for gasoline engines

Jianxiong Wu<sup>1</sup>, Jean-Philippe Dacquin<sup>1</sup>, Nora Djelal<sup>1</sup>,  
Catherine Cordier<sup>2</sup>, Christophe Dujardin<sup>1</sup>, Pascal Granger<sup>1\*</sup>

<sup>1</sup> Univ. Lille, CNRS, Centrale Lille, Univ. Artois, UMR 8181 - UCCS - Unité de Catalyse et Chimie du Solide, F-59000 Lille, France

<sup>2</sup> Univ. Lille, CNRS, INRAE, Centrale Lille, UMR8207 – UMET - Unité Matériaux Et Transformations, F-59000 Lille, France

---

\* Corresponding author : Email [pascal.granger@univ-lille.fr](mailto:pascal.granger@univ-lille.fr)  
Phone number : +33 320 434 938

## **Abstract**

Calcium and copper substitutions, in A-site and B-site respectively, of parent stoichiometric  $\text{LaFeO}_3$  and La-deficient  $\text{La}_{0.7}\text{FeO}_3$  perovskites led to significant improvements in the kinetics of CO and propene oxidation in typical three-way operating conditions. La-deficient  $\text{La}_{0.7}\text{Fe}_{1-y}\text{Cu}_y\text{O}_3$  perovskites were found more prone to surface copper oxide segregation leading to more active extra-framework copper oxide species in CO oxidation. Optimal performances were obtained on  $\text{La}_{0.7}\text{Fe}_{0.8}\text{Cu}_{0.2}\text{O}_3$  composition. At higher Cu content, strong copper agglomeration leads to deactivation. More stable systems were obtained on dual substituted samples thanks to calcium substitution stabilizing copper inside the perovskite lattice and slowing down subsequent surface agglomeration. Rate enhancements in propene oxidation is observed on A-site deficient  $\text{La}_{0.6}\text{Ca}_x\text{Fe}_{0.8}\text{Cu}_{0.2}\text{O}_3$  with  $x \leq 0.2$  but a sharp loss in rate is observed on stoichiometric  $\text{La}_{0.6}\text{Ca}_{0.4}\text{Fe}_{0.8}\text{Cu}_{0.2}\text{O}_3$  perovskite explained by a progressive shift from suprafacial to intrafacial mechanism involving in this latter case the redox  $\text{Fe}^{4+}/\text{Fe}^{3+}$  couple and lattice oxygen species.

**Keywords** : Perovskites, Three-Way-Catalyst, La-deficient  $\text{La}_{1-x}\text{FeO}_3$ , Dual calcium copper substitution, CO and propene oxidation.

## 1. Introduction

First attempt in the use of perovskite-based materials in post-combustion catalysis was pointed out in 1974 highlighting promising oxidative properties to convert CO and unburnt hydrocarbons [1]. The development of perovskite based two-way catalysts at the beginning of the 70s represented a significant breakthrough avoiding an extensive use of Platinum Group Metals (PGM). Their peculiar oxidative properties have been more recently highlighted in Diesel Oxidation Catalysts (DOC) for oxidizing NO to NO<sub>2</sub> showing that perovskites can rival with platinum [2].

The unique physicochemical properties of ABO<sub>3</sub> perovskite type structures lie in the adjustments of valency and vacancy thanks to partial substitutions of A- and B-sites. All these changes can alter differently their selective catalytic properties. Basically, the ABO<sub>3</sub> structure of perovskite can accommodate a wide number of components and stabilize various distorted structures. The stability of the structure depends directly on the geometrical constraints of octahedral and dodecahedral cavities. The flexibility of these mixed-oxide materials is also related to the creation of electronic imbalances through the substitution of trivalent by divalent cations which can induce the stabilization of substituted B-site cations in unusual oxidation states.

Several academic works pointed out their potential applications for NO removal [3]. However, previous attempts revealed that the balance between oxidative and reductive properties to promote their use as three-way catalyst (TWC) is still a challenging issue [4,5]. Recent developments of composite materials consisting in the deposition of CuO copper oxide on perovskite structures [6] as well as the implementation of innovative methodologies for developing their specific surface area through reactive grinding [7,8] and more recently from Flame-Spray-Pyrolysis (FSP) [9] underlined their potentialities. However, these

approaches are not fully mature to envision commercial developments at short terms. Indeed, despite sharp gain in specific surface area  $\sim 80 \text{ m}^2/\text{g}$ , it was found that the catalytic performances of commercial PdRh TWC sharply outperform those measured on perovskite in simulated gasoline exhaust feed. As a matter of fact, practical developments were essentially obtained thanks to the incorporation of low amount of PGM in perovskite. The self-regenerative behavior of perovskites can protect nano-sized PGM particles to thermal sintering in comparison to alumina support [10,11] and led to superior performances during cold start.

Today, perovskite type materials are still attractive as post-combustion catalysts because of high tolerance to sulfur poisoning [12,13] and a growing interest related to successful achievements in soot oxidation with efficiency related to the density of suprafacial oxygen species [14,15]. These properties could be useful to fulfill more stringent standard regulations and comply new Euro 6c regulations. They have recently arisen and should account for the removal of small suspended particle emissions from gasoline engines keeping the other atmospheric pollutants at their lowest limit. Accordingly, improved technologies are expected combining particulate filter and TWC [16,17].

Previous investigations demonstrated that a sharp gain in activity can be obtained on La-deficient  $\text{LaFeO}_3$  in simulated TWC feed gas in comparison to the stoichiometric counterpart. This trend has been related to lower lanthanum enrichment jointly with improved redox properties of Fe(+III) species [18]. Previous investigations also revealed that A-deficient cubic phases are more stable than their stoichiometric counterparts [19]. Stoichiometric and La-deficient  $\text{LaFeO}_3$  served as parent perovskite compositions in this study to investigate subsequent calcium and copper substitutions. The selection of calcium was earlier suggested from theoretical calculations which found that Ca-doping can induce an increase in oxygen vacancies which can lead to enhanced ionic conductivity [20]. The ability of such materials to

create defective sites is also essential because it would be possible to modulate their intrinsic catalytic properties. The presence of ionic vacancies can be also a criterion in determining the extent of the self-regenerative behavior characteristic for this variety of mixed-oxides.

Regarding copper substitution in iron-based perovskites, it has been widely regarded as the most active candidates among the first transition element series for NO reduction by CO [21]. It was found that the activity of  $\text{La}_2\text{CuO}_4$  for NO reduction could be enhanced by partial substitution of copper by iron due to the promotion of cationic  $\text{Cu}^{2+}$  dispersion. Particular attention in this present study will be paid to copper dispersion/aggregation processes in connection with calcium substitution as a potential strategy to monitor the copper dispersion and the related catalytic properties for CO and propene oxidation.

## **2. Experimental**

### *2.1. Catalyst preparation*

Conventional citric method was used for the synthesis of parent and dual substituted perovskites. This method, based upon the sol-gel route proposed by Taguchi et al. [22], used citric acid as chelating agent. Metal nitrate precursors were dissolved in an aqueous solution and then mixed with equal molar amount of citric acid. The solvent was subsequently removed in a rotary evaporator in moderate operating conditions (heating temperature of 60 °C, rotating velocity of 30 rpm) to obtain gelation. The gel thus obtained was dried in a static oven at 80 °C for 48 h. The dried solid was finally calcined in air at 600 °C for 8 h with a temperature ramp of 2 °C/min.

### *2.2. Physicochemical characterization*

Powder X-ray diffraction (XRD) experiments were performed at room temperature using a Bruker AXS D8 diffractometer (Cu K $\alpha$  source,  $\lambda = 0.154$  nm). Diffraction data were collected in the  $2\theta$  range of 5-120 degree with a step of 0.02 degree. Unit cell parameters were calculated by means of Rietveld refinement method. The crystal size was calculated by Williamson-Hall approach using LaB<sub>6</sub> as standard. Standard deviations were obtained by Bérar correction.

*Ex situ* Mössbauer spectroscopic measurements were carried out at room temperature using a <sup>57</sup>Co (Rh) source. Data fitting was conducted with Lorentzian shape peaks. Pure iron foil served as reference for the calculation of hyperfine parameters: hyperfine field (HF), isomer shift (IS), quadrupole splitting (QS).

Scanning Electron Microscopy (SEM) analysis was performed on a Hitachi S-4700 Cold Field Emission Gun Scanning Electron Microscope operating at an acceleration voltage of 15 kV with a resolution of 1.5 nm. Energy-dispersive X-ray spectroscopy (EDS) was implemented for conducting elemental analysis. Oxford EDS system was employed for these analyzes.

H<sub>2</sub>-Temperature-Programmed Reduction (H<sub>2</sub>-TPR) experiments were performed on a Micromeritics AutoChem 2920 analyzer. Typically, 50 mg sample was exposed to a 50 mL/min flowrate of 5 vol.% H<sub>2</sub> in Ar and gradually heated to 1000 °C with a heating rate of 5 °C/min. A thermal conductivity detector was employed to monitor the evolution of hydrogen concentration. O<sub>2</sub>-Temperature-Programmed-Desorption (O<sub>2</sub>-TPD) experiments were conducted on the same apparatus. Prior measurements, 50 mg sample was preheated in pure oxygen at 600 °C for 1 h and then cooled down to room temperature. After a purge in Helium at room temperature, the sample was submitted to a temperature ramp up to 1000 °C

with  $dT/dt = 10\text{ }^{\circ}\text{C}/\text{min}$ . Outlet gas was analyzed by using thermal Conductivity Detector and mass spectrometer ( $m/z = 32$ ).

Textural properties were examined by nitrogen physisorption at  $-196\text{ }^{\circ}\text{C}$  using a Micromeritics Tristar analyzer. Prior to measurements, the samples were outgassed under vacuum for 4 h. Specific surface area (SSA) was calculated according to the Brunauer-Emmett-Teller (BET) theory and pore size distribution based upon the Barret-Joyner-Halenda (BJH) theory.

X-ray photoelectron spectroscopy (XPS) analysis was performed with a Kratos Axis Ultra spectrometer. This instrument was equipped with a monochromatized Al  $K\alpha$  source (15 mA, 14 kV) and a charge compensation gun. Binding Energy values were corrected by using the C 1s core level as reference at 284.8 eV. Spectral analysis was carried out using Casa XPS software. A mixed Gaussian/Lorentzian (70/30) line profile was adopted for peak deconvolution. Calculations of surface atomic composition were conducted by relative sensitivity factor analysis method by using Shirley background subtraction type.

### *2.3. Catalytic measurements*

Temperature-Programmed-Reaction experiments (TPR) were carried out in a fixed bed flow reactor at atmospheric pressure from 110 to 550  $^{\circ}\text{C}$ . 200 mg catalyst in powder form with average grain size of 150  $\mu\text{m}$  were mixed with the same amount of SiC. The total inlet volumetric flowrate ( $Q_0$ ) was fixed to 12  $\text{L h}^{-1}$ , corresponding to a  $Q_0/W$  of 60,000  $\text{mL h}^{-1}\text{ g}^{-1}$ . A heating rate of 5  $^{\circ}\text{C min}^{-1}$  and cooling rate of 10  $^{\circ}\text{C min}^{-1}$  were adopted during heating-up and cooling-down respectively. As described in Fig. S1 in Supplementary Information (SI), successive temperature-programmed reaction experiments were conducted in stoichiometric, lean and rich conditions according to the compositions reported in Table S1 in

SI. The composition of the outlet gas mixtures was monitored by a Thermo Scientific Model 42i-HL chemiluminescence NO<sub>x</sub> analyzer and an Agilent 490 Micro Gas Chromatography for the detection and the quantification of N<sub>2</sub>, N<sub>2</sub>O, O<sub>2</sub>, CO, C<sub>3</sub>H<sub>6</sub> and C<sub>3</sub>H<sub>8</sub>. Kinetic exploitation was described in Supplementary Information taking the mass balance equation of a plug flow reactor into account. Eqs. (S1)-(S3) were established for the calculation of the rate constant  $k$ , the specific and the normalized reaction rate,  $r_{\text{spec}}$  and  $r_{\text{norm}}$ , respectively. These calculations also referred to previous verifications showing that external and internal mass transfer phenomena should not occur significantly for conversion lower than 0.4 verifying the boundary conditions given by Eq. (S4) in SI.

### 3. Results

#### 3.1. Bulk characterization

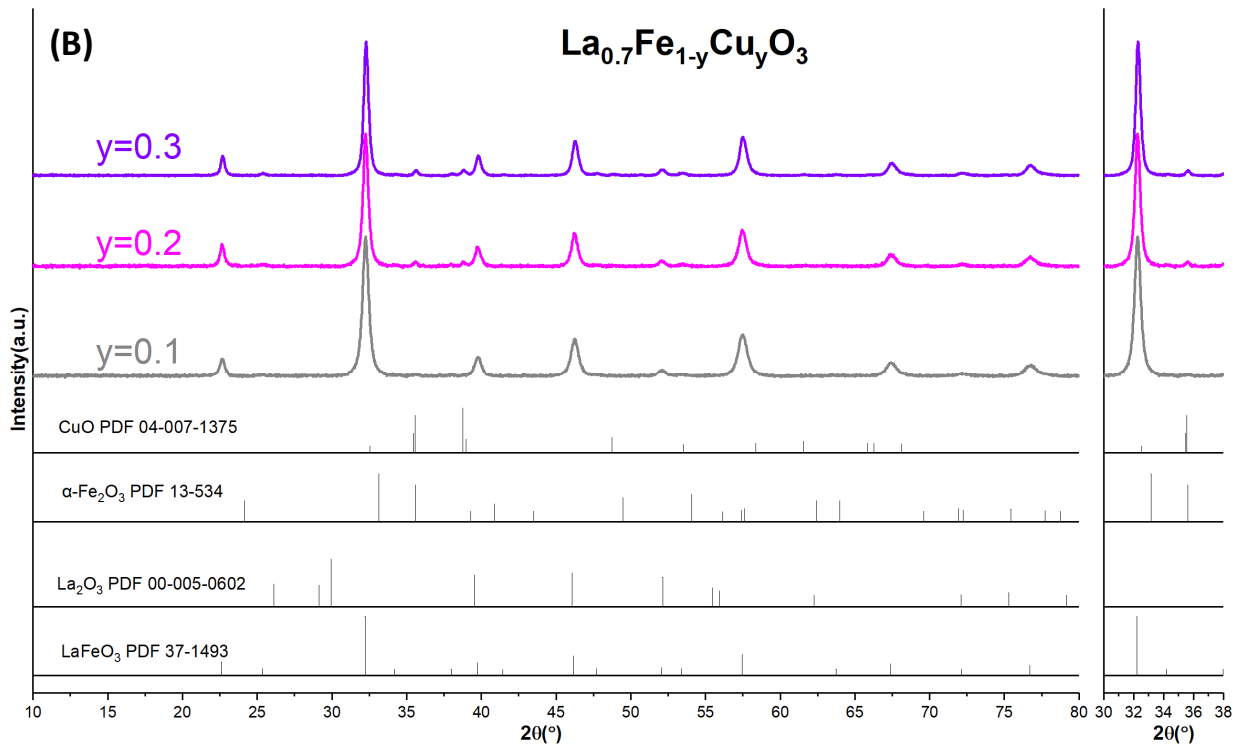
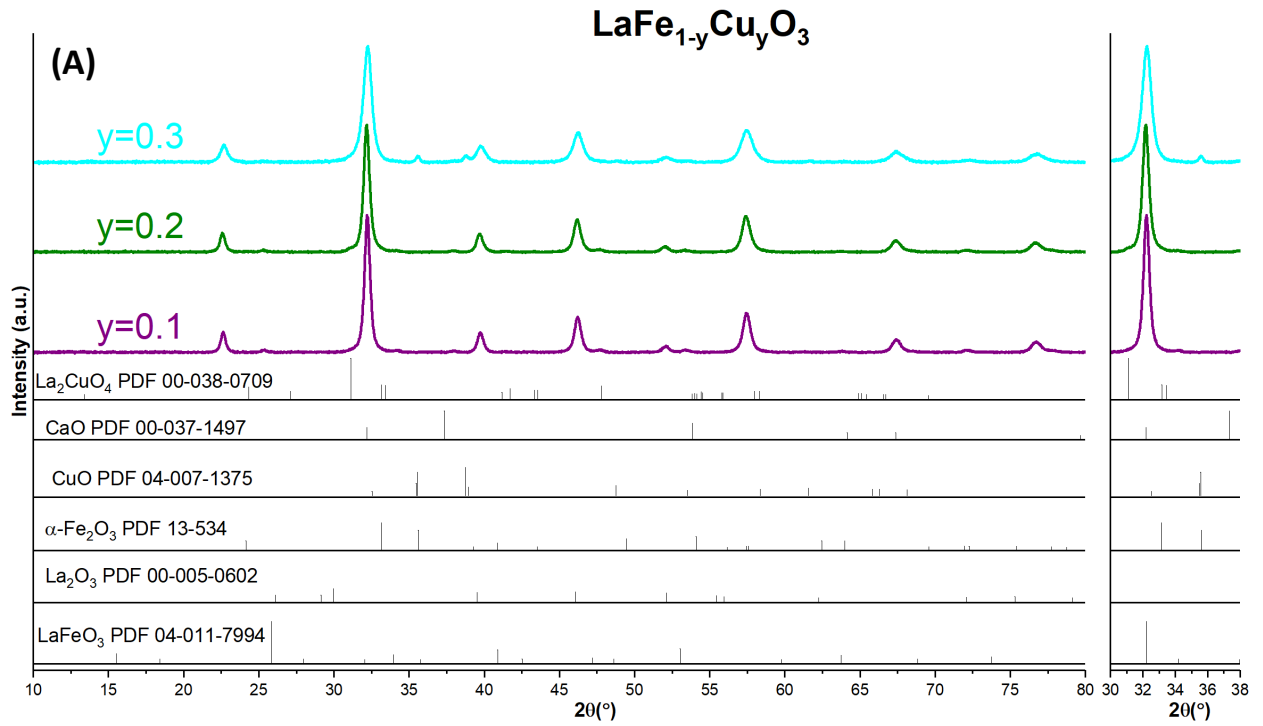
##### 3.1.1. X-ray diffraction analysis

XRD patterns recorded on the parent perovskites LaFeO<sub>3</sub> and La<sub>0.7</sub>FeO<sub>3</sub>, calcined in air at 600°C, are reported in Fig. S2 (SI). The most intense reflections characterize an orthorhombic structure with the space group Pnma (PDF 37-1493). Additional weak reflections are discernible at  $2\theta = 33.2^\circ$  and  $35.6^\circ$  underlining a minor segregation of  $\alpha$ -Fe<sub>2</sub>O<sub>3</sub> phase on La<sub>0.7</sub>FeO<sub>3</sub>. Subsequent iron substitution by copper in stoichiometric LaFeO<sub>3</sub> induces a slight shift of the (121) reflection towards higher  $2\theta$  angles at increasing copper concentration (see Fig. 1(A)). Jointly, additional (-111) and (111) reflections at  $2\theta = 35.6^\circ$  and  $38.8^\circ$  characteristic of CuO (PDF 04-007-1375) appear reflecting the formation of extra-framework copper oxide species. On the other hand, the presence of La<sub>2</sub>CuO<sub>4</sub> has not been detected. The

orthorhombic structure of the parent materials still predominates on single and dual-substituted samples.

The calculation of the structural parameters and cell volume only evidences marginal changes on  $\text{LaFe}_{1-y}\text{Cu}_y\text{O}_3$  as previously reported [23]. A weak contraction effect on the cell unit volume appears for  $y = 0.3$  which *a priori* contradicts the predicted expansion effect with respect to the higher ionic radius of  $\text{Cu}^{2+}$  than that of  $\text{Fe}^{3+}$  (0.72 Å vs. 0.64 Å respectively). As a matter of fact, this expansion could be counterbalanced by oxygen release with related formation of ionic vacancies inducing a contraction effect on the perovskite structure. Let us note that the formation of extra-framework copper oxide species could partly explain the weak deviations observed. The same tendencies appear on XRD patterns recorded Cu-substituted La-deficient  $\text{La}_{0.7}\text{Fe}_{1-y}\text{Cu}_y\text{O}_3$  perovskites. However, it is obvious that an intensification of the reflections assigned to CuO at lower Cu content likely reflects a faster formation of extra-framework copper oxide species.

Fig. 1(C) shows a slight shift towards higher  $2\theta$  values on the main reflections with a rise in Ca concentration more accentuated on the stoichiometric  $\text{La}_{0.6}\text{Ca}_{0.4}\text{Fe}_{0.8}\text{Cu}_{0.2}\text{O}_3$  composition suggesting more extensive lattice distortions. Data in Table 1 clearly indicate a significant contraction of the unit cell volume as reported elsewhere [24,25]. According to comparable  $\text{La}^{3+}$  and  $\text{Ca}^{2+}$  ionic radii (1.36 Å vs. 1.34 Å respectively), such structural changes would be more related to a greater stabilization of  $\text{Fe}^{4+}$  to compensate charge imbalance created by Ca substitution. Indeed, a lower ionic radius characterizes  $\text{Fe}^{4+}$  compared  $\text{Fe}^{3+}$ , i.e. 0.585 Å vs. 0.685 Å for  $\text{Fe}^{3+}$ . Let us note the absence of a CaO phase on all the calcium and copper doped perovskites.



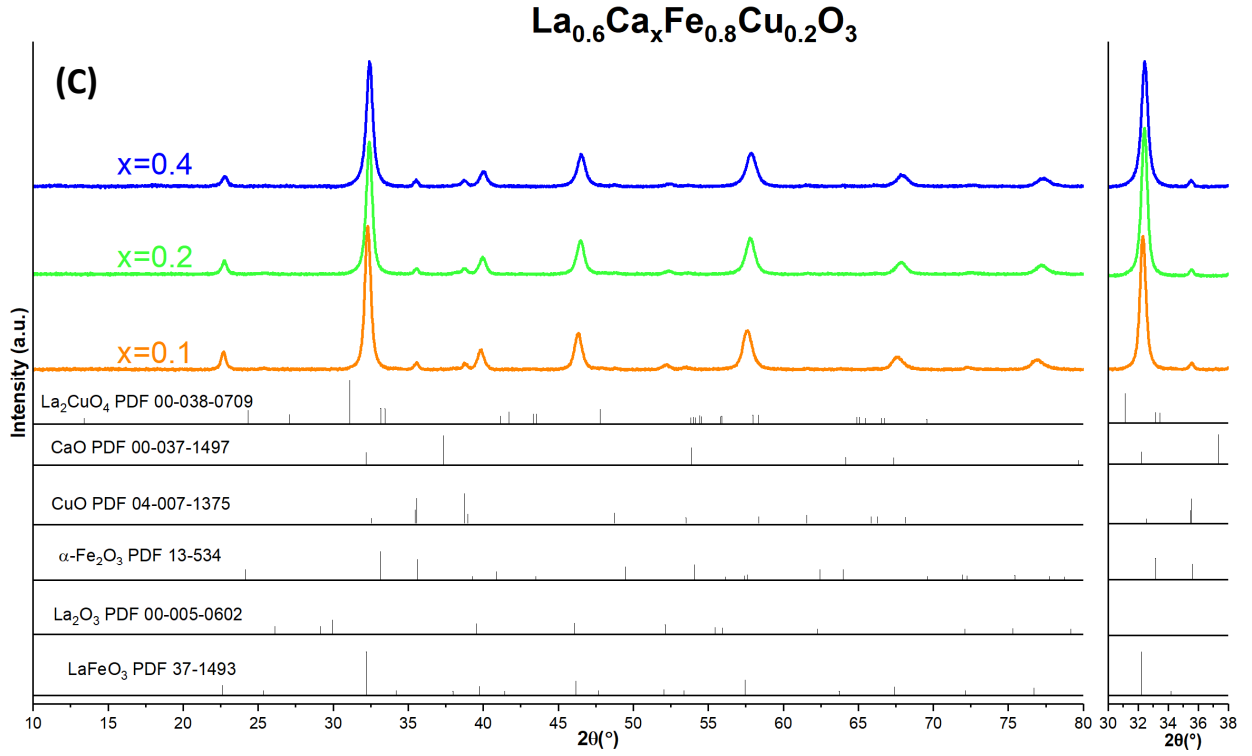


**Fig. 1.** X-ray diffractograms for stoichiometric LaFe<sub>1-y</sub>Cu<sub>y</sub>O<sub>3</sub> (A), La-deficient La<sub>0.7</sub>Fe<sub>1-y</sub>Cu<sub>y</sub>O<sub>3</sub> (B) and Ca-substituted perovskites La<sub>0.6</sub>Ca<sub>x</sub>Fe<sub>0.8</sub>Cu<sub>0.2</sub>O<sub>3</sub> (C).

**Table 1.** Structural features including lattice parameters on dual substituted stoichiometric LaFeO<sub>3</sub> and La-deficient La<sub>1-x</sub>FeO<sub>3</sub> parent perovskite.

Catalysts	Crystal system	a(Å) <sup>a</sup>	b(Å) <sup>a</sup>	c(Å) <sup>a</sup>	unit cell <sup>a</sup> volume(Å <sup>3</sup> )	Crystallite size (nm) <sup>b</sup>
LaFeO <sub>3</sub>	orthorhombic	5.560(1)	7.861(0)	5.557(1)	242.88±0.05	29.4
La <sub>0.7</sub> FeO <sub>3</sub>	orthorhombic	5.560(0)	7.878(1)	5.535(1)	242.44±0.03	21.7
LaFe <sub>0.9</sub> Cu <sub>0.1</sub> O <sub>3</sub>	orthorhombic	5.561(1)	7.849(1)	5.554(1)	242.49±0.03	31.2
LaFe <sub>0.8</sub> Cu <sub>0.2</sub> O <sub>3</sub>	orthorhombic	5.572(1)	7.837(0)	5.557(1)	242.69±0.02	33.6
LaFe <sub>0.7</sub> Cu <sub>0.3</sub> O <sub>3</sub>	orthorhombic	5.557(0)	7.863(1)	5.533(0)	241.82±0.06	25.7
La <sub>0.7</sub> Fe <sub>0.9</sub> Cu <sub>0.1</sub> O <sub>3</sub>	orthorhombic	5.557(0)	7.868(1)	5.532(1)	241.90±0.02	24.3
La <sub>0.7</sub> Fe <sub>0.8</sub> Cu <sub>0.2</sub> O <sub>3</sub>	orthorhombic	5.545(1)	7.857(1)	5.550(1)	241.80±0.05	28.6
La <sub>0.7</sub> Fe <sub>0.7</sub> Cu <sub>0.3</sub> O <sub>3</sub>	orthorhombic	5.561(0)	7.829(1)	5.543(0)	241.37±0.02	42.3
La <sub>0.6</sub> Ca <sub>0.1</sub> Fe <sub>0.8</sub> Cu <sub>0.2</sub> O <sub>3</sub>	orthorhombic	5.544(1)	7.837(1)	5.539(0)	240.66±0.03	32.5
La <sub>0.6</sub> Ca <sub>0.2</sub> Fe <sub>0.8</sub> Cu <sub>0.2</sub> O <sub>3</sub>	orthorhombic	5.542(0)	7.785(0)	5.531(0)	238.63±0.03	30.4
La <sub>0.6</sub> Ca <sub>0.4</sub> Fe <sub>0.8</sub> Cu <sub>0.2</sub> O <sub>3</sub>	orthorhombic	5.525(0)	7.810(0)	5.436(1)	234.56±0.06	24.4

<sup>a</sup> lattice parameter and unit cell volume calculated from the Rietveld refinement method

<sup>b</sup> crystal size was calculated by the Williamson-Hall plot method using LaB<sub>6</sub> as standard specimen

### 3.1.2. Mössbauer spectroscopy

The fitting of the Mössbauer spectra recorded at 20 °C (Fig. S3 in SI) gives an estimation of the Isomer Shift (IS), the Quadrupole Splitting (QS) and the Hyperfine magnetic Field (HF). These hyperfine parameters provide information on the nature and coordination geometry of each iron ion species as well as their relative abundance, their electronic density and magnetic state.

Several sextets have been superimposed in the spectral data fitting corresponding to different positions of cationic iron species in distorted or undistorted octahedron as well as tetrahedron. Their relative abundances in Table 2 have been calculated according to a binomial distribution as suggested by Russo et al. [26]. High spin  $\text{Fe}^{4+}$  ( $S = 2$ ) with an Isomer Shift of +0.07 mm/s is also detected on the stoichiometric  $\text{LaFeO}_3$  parent material which could be stabilized in square pyramidal coordination corresponding to an easier intergrowth with octahedral layer as reported elsewhere [27]. On the other hand, the absence of  $\text{Fe}^{4+}$  and a lower abundance of  $\text{Fe}^{(3+\delta)+}$  are noticeable on  $\text{La}_{0.7}\text{FeO}_3$  which suggests that electroneutrality would be merely maintained through the creation of oxygen vacancies for perovskites with A-site atom deficiency. Similarly to  $\text{LaFeO}_3$ , the stoichiometric perovskite  $\text{LaFe}_{0.8}\text{Cu}_{0.2}\text{O}_3$  containing 20 at.% copper doping in B site yielded a broader spectrum and higher  $\text{Fe}^{4+}$  ratio (8.59%;  $\text{Fe}^{4+}$  high spin), implying that the main mechanism of charge compensation is achieved through both the stabilization of higher valence of B-site atom and the oxygen vacancies generated within the lattice. Subsequent copper substitution of  $\text{La}_{0.7}\text{FeO}_3$  exhibits similar trends depicted on the parent  $\text{La}_{0.7}\text{FeO}_3$  sample suggesting that charge compensation through the formation of anionic vacancies prevails.

More significant broadening appears distinctly on the spectra recorded on dual-substituted samples reflecting significant structural deformations. This is well illustrated from the comparison of the relative abundances in Table 2 showing that Ca incorporation is accompanied to a relative increase of  $\text{Fe}^{3+}$  stabilized in tetrahedral coordination at the expense

of Fe<sup>3+</sup> coordinated in undistorted octahedron centers. Such a comparison is also true by comparing the abundance of undistorted and distorted octahedron sites but in lower extent. As calcium doping induces significant charge imbalances, then the formation of Fe<sup>4+</sup> should be in principle expected. Such a trend has been previously reported but essentially for stoichiometric compositions. Higher ratio of Fe<sup>3+</sup> cations present in the distorted octahedral centers has been predominantly observed, signifying more tilting of the [FeO<sub>6</sub>] octahedron and greater lattice disorder in agreement with previous XRD analysis. On the other hand, the formation of Fe<sup>4+</sup> does not occur on La-deficient La<sub>0.6</sub>Ca<sub>x</sub>Fe<sub>0.8</sub>Cu<sub>0.2</sub>O<sub>3</sub> materials. It is worth noting that Fe<sup>4+</sup> species were found only in the stoichiometric La<sub>0.6</sub>Ca<sub>0.4</sub>Fe<sub>0.8</sub>Cu<sub>0.2</sub>O<sub>3</sub> composition. As discussed, the lack of detection of Fe<sup>4+</sup> for the La-deficient perovskites indicates that electroneutrality is preferentially kept through the creation of anionic vacancies, which may improve the oxygen storage capacity closely associated with the redox features of these catalysts. Less structural disorders of the La-deficient perovskites with greater stabilization of cationic iron species in undistorted octahedron than on stoichiometric specimen, i.e. 86.1% vs. 35.1% on La<sub>0.6</sub>Ca<sub>0.4</sub>Fe<sub>0.8</sub>Cu<sub>0.2</sub>O<sub>3</sub>, also reflect a greater structural stability of the orthorhombic structure for La<sub>0.6</sub>Ca<sub>0.2</sub>Fe<sub>0.8</sub>Cu<sub>0.2</sub>O<sub>3</sub> compared to La<sub>0.6</sub>Ca<sub>0.4</sub>Fe<sub>0.8</sub>Cu<sub>0.2</sub>O<sub>3</sub>. A similar comparison was previously established on cubic perovskite structure [19].

**Table 2.** Hyperfine parameters from Mössbauer spectroscopy analysis at room temperature of single and dual substituted LaFeO<sub>3</sub> and La-deficient La<sub>0.7</sub>FeO<sub>3</sub> perovskites.

Catalyst	Iron species	Coordination geometry	Valency	HF (T) ± 0.1T	IS (mm/s) ± 0.05 mm/s	QS (mm/s) ± 0.05 mm/s	Relative abundance (%)
LaFeO <sub>3</sub>	Fe <sup>3+</sup>	Undistorted octahedron	2.8	55.0	0.57	-0.41	4.83
			3.29	51.9	0.37	-0.04	61.71
			3.35	48.1	0.32	-0.33	5.34
			2.7	47.7	0.58	0	6.68
	Fe <sup>3+</sup>	Distorted octahedron	3.4	-	0.30	0.38	11.35
Fe <sup>3+δ</sup>	Tetrahedron	3.8	-	0.14	0.16	5.26	

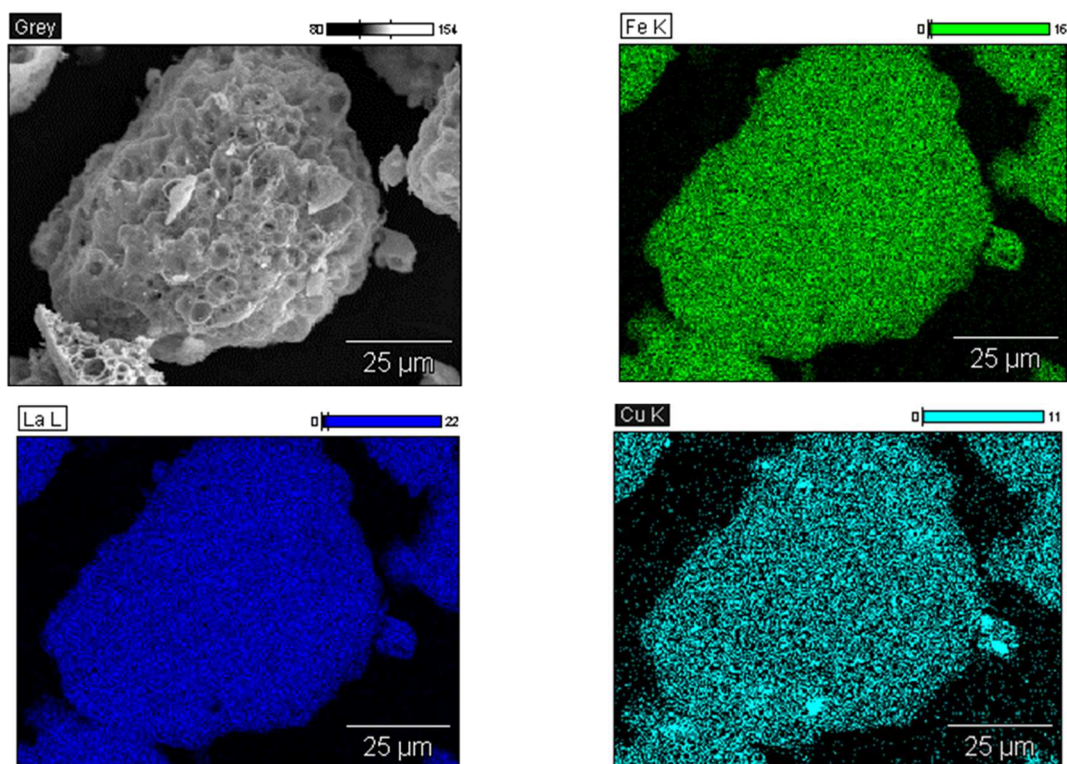
	Fe <sup>4+</sup>	High spin	4	37.0	0.07	-0.32	4.83
			3.20	51.6	0.37	-0.01	52.35
	Fe <sup>3+</sup>	Undistorted octahedron	3.30	49.8	0.34	-0.02	13.87
			3.20	48.7	0.38	0.13	4.10
			3.00	46.3	0.48	0.02	7.40
La <sub>0.7</sub> FeO <sub>3</sub>			3.05	42.2	0.45	0.07	5.04
	Fe <sup>3+</sup>	Distorted octahedron	3.00	18.9	0.48	-0.02	4.78
			3.10	16.0	0.44	0.02	4.77
			3.00	-	0.47	0.78	3.10
			3.30	-	0.35	0.32	2.48
	Fe <sup>3+δ</sup>	Tetrahedron	3.80	-	0.13	0.38	2.11
			3.3	51.8	0.36	-0.02	59.42
	Fe <sup>3+</sup>	Undistorted octahedron	3.3	49.9	0.34	-0.07	12.73
			2.7	47.4	0.59	-0.15	6.63
			2.9	40.5	0.50	0.15	0.84
LaFe <sub>0.8</sub> Cu <sub>0.2</sub> O <sub>3</sub>	Fe <sup>3+</sup>	Distorted octahedron	3.3	-	0.35	0.40	8.98
	Fe <sup>3+</sup>	Tetrahedron	3.75	-	0.16	0.24	2.81
	Fe <sup>4+</sup>	High spin	3.9	46.2	0.11	-0.19	4.41
			4.5	38.6	-0.15	-0.35	4.18
			3.18	50.9	0.36	-0.05	16.65
	Fe <sup>3+</sup>	Undistorted octahedron	3.22	49.5	0.33	-0.03	25.08
			3.23	46.9	0.32	-0.02	22.54
			3.30	42.9	0.28	-0.06	12.21
La <sub>0.7</sub> Fe <sub>0.8</sub> Cu <sub>0.2</sub> O <sub>3</sub>	Fe <sup>3+</sup>	Distorted Octahedron	3.00	-	0.50	1.01	10.64
	Fe <sup>(3+δ)+</sup>	Tetrahedron	3.38	35.6	0.23	-0.01	7.19
			3.36	-	0.24	0.28	5.69
			3.18	51.7	0.36	-0.00	23.45
	Fe <sup>3+</sup>	Undistorted octahedron	3.18	50.6	0.36	-0.02	35.82
			3.25	47.5	0.32	-0.00	11.91
			3.27	43.9	0.39	-0.05	8.98
La <sub>0.6</sub> Ca <sub>0.1</sub> Fe <sub>0.8</sub> Cu <sub>0.2</sub> O <sub>3</sub>			3.09	36.9	0.41	-0.17	6.09
	Fe <sup>3+</sup>	Distorted Octahedron	2.98	-	0.48	0.85	8.62
	Fe <sup>(3+δ)+</sup>	Tetrahedron	3.22	-	0.23	0.33	5.13
			3.20	50.7	0.35	-0.03	17.02
	Fe <sup>3+</sup>	Undistorted octahedron	3.20	49.7	0.34	-0.01	24.68
			3.12	46.9	0.39	-0.04	21.35
			3.10	43.5	0.41	-0.00	14.00
La <sub>0.6</sub> Ca <sub>0.2</sub> Fe <sub>0.8</sub> Cu <sub>0.2</sub> O <sub>3</sub>			3.21	38.3	0.34	-0.04	9.01
	Fe <sup>3+</sup>	Distorted octahedron	3.00	-	0.46	0.42	9.05
	Fe <sup>(3+δ)+</sup>	Tetrahedron	3.40	-	0.21	0.21	4.89
La <sub>0.6</sub> Ca <sub>0.4</sub> Fe <sub>0.8</sub> Cu <sub>0.2</sub> O <sub>3</sub>	Fe <sup>3+</sup>	Undistorted	3.25	49.6	0.31	0.01	13.07

	octahedral	3.05	44.3	0.44	-0.12	22.00
Fe <sup>3+</sup>	Distorted octahedron	3.21	40.0	0.34	0.21	12.30
Fe <sup>(3+δ)+</sup>	Tetrahedron	3.39	47.7	0.22	0.07	20.67
		3.43	34.2	0.19	0.01	6.69
Fe <sup>3+</sup>	tetrahedron or distorted octahedron	3.27	-	0.30	0.48	7.96
Fe <sup>4+</sup>	High spin	3.50	39.9	0.15	-0.17	12.75
		3.60	-	0.09	0.36	4.56

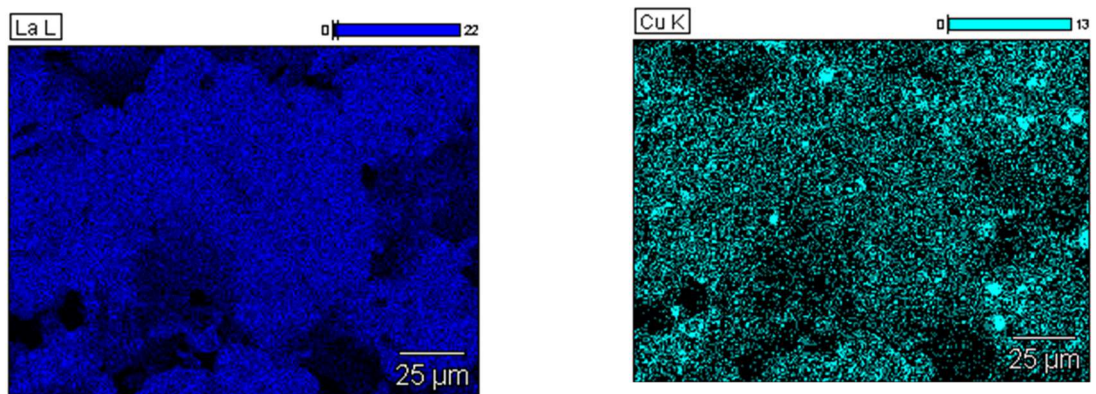
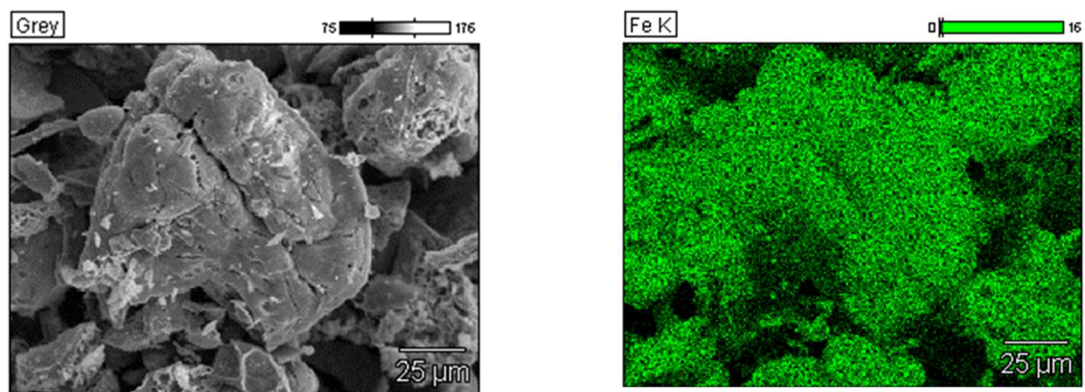
### 3.1.3. Scanning Electron Microscopy (SEM) coupled to Energy Dispersive Spectroscopy (EDS) analysis

SEM analysis was performed on parent stoichiometric and La-deficient benchmarks (see Figs. S4(A) and (B) in SI as well as on substituted samples by calcium and iron illustrated in Fig. S4(C) in SI and Figs. 2-5. Energy Dispersive X-ray Spectroscopy was used to analyze the different elements with elemental composition reported in Table 3. Elemental mapping analysis also provides the distribution of these elements on a small volume in accordance with the scale indicated in Figs. 2-5. As seen, SEM images reveal different morphologies and different degrees of aggregation according to the composition (Figs. S4(A) and (B) in SI). Smaller grains are observable on La<sub>0.7</sub>FeO<sub>3</sub> compared to the stoichiometric counterpart. Further, substitutions with calcium and copper do not lead to more organization in terms of size and morphology of the grain. The scale selected for analyzing LaFeO<sub>3</sub> and La<sub>0.7</sub>FeO<sub>3</sub> does not reveal strong heterogeneity in composition in the volume analyzed. An homogeneous distribution of La and Fe is observable which agree with the prevalence of the orthorhombic structure of the perovskite and the absence of bulk impurities in agreement with XRD analysis. On the other hand, the introduction of copper emphasizes the fact that Cu(+II) species are not be randomly distributed as expected because copper aggregates appear more distinctly on La<sub>0.7</sub>Fe<sub>0.8</sub>Cu<sub>0.2</sub>O<sub>3</sub> (see Fig. 2). It is worthwhile to note that no aggregation of lanthanum and iron is discernible which still agrees with XRD analysis underlining the

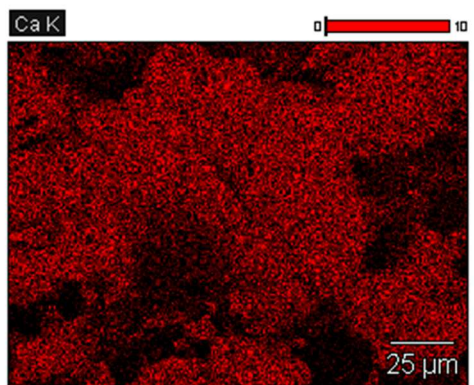
conservation of the orthorhombic structure and formation of bulk CuO species. SEM-EDS images for Ca-doped samples reveal on La-deficient samples containing low calcium concentration the same large spots indicating the formation of extra-framework copper oxide species. In contrast, at increasing calcium content, *i.e.*  $\text{La}_{0.6}\text{Ca}_{0.2}\text{Fe}_{0.8}\text{Cu}_{0.2}\text{O}_3$ , Cu mapping does not reveal the presence of large spot reflecting significant heterogeneity in copper distribution. Such an observation would suggest that calcium likely slower copper segregation process in qualitative agreement with XRD analysis showing the absence of bulk CaO and lower aggregation of CuO at increasing calcium content. Elemental analysis seems also supporting this explanation showing a better agreement between Cu/Fe atomic ratio at short and long range from EDS and ICP-OES analysis. On the other hand, the restoration of small patches on copper mapping on  $\text{La}_{0.6}\text{Ca}_{0.4}\text{Fe}_{0.8}\text{Cu}_{0.2}\text{O}_3$  indicates an aggregation of copper which seems consistent with a lower structural stability compared to dual substituted La-deficient perovskites.

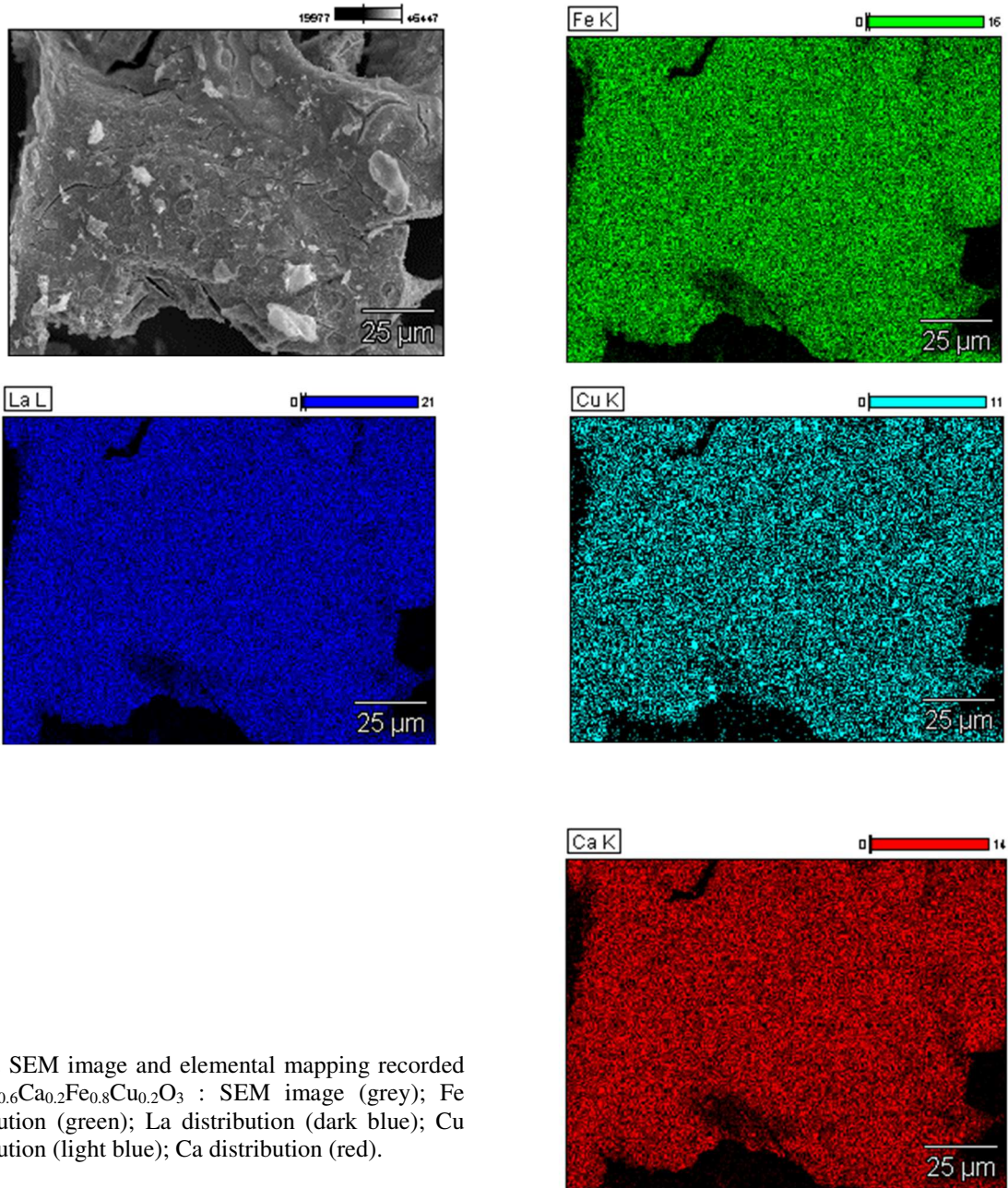


**Fig. 2.** SEM image and elemental mapping recorded on  $\text{La}_{0.7}\text{Fe}_{0.8}\text{Cu}_{0.2}\text{O}_3$ : SEM image (grey); Fe distribution (green); La distribution (dark blue); Cu distribution (light blue).

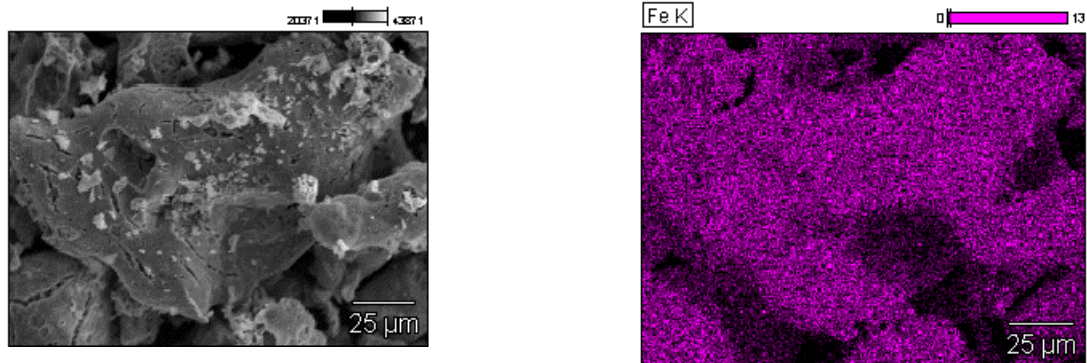


**Fig. 3.** SEM image and elemental mapping recorded on  $\text{La}_{0.6}\text{Ca}_{0.1}\text{Fe}_{0.8}\text{Cu}_{0.2}\text{O}_3$  : SEM image (grey); Fe distribution (green); La distribution (dark blue); Cu distribution (light blue).





**Fig. 4.** SEM image and elemental mapping recorded on  $\text{La}_{0.6}\text{Ca}_{0.2}\text{Fe}_{0.8}\text{Cu}_{0.2}\text{O}_3$  : SEM image (grey); Fe distribution (green); La distribution (dark blue); Cu distribution (light blue); Ca distribution (red).



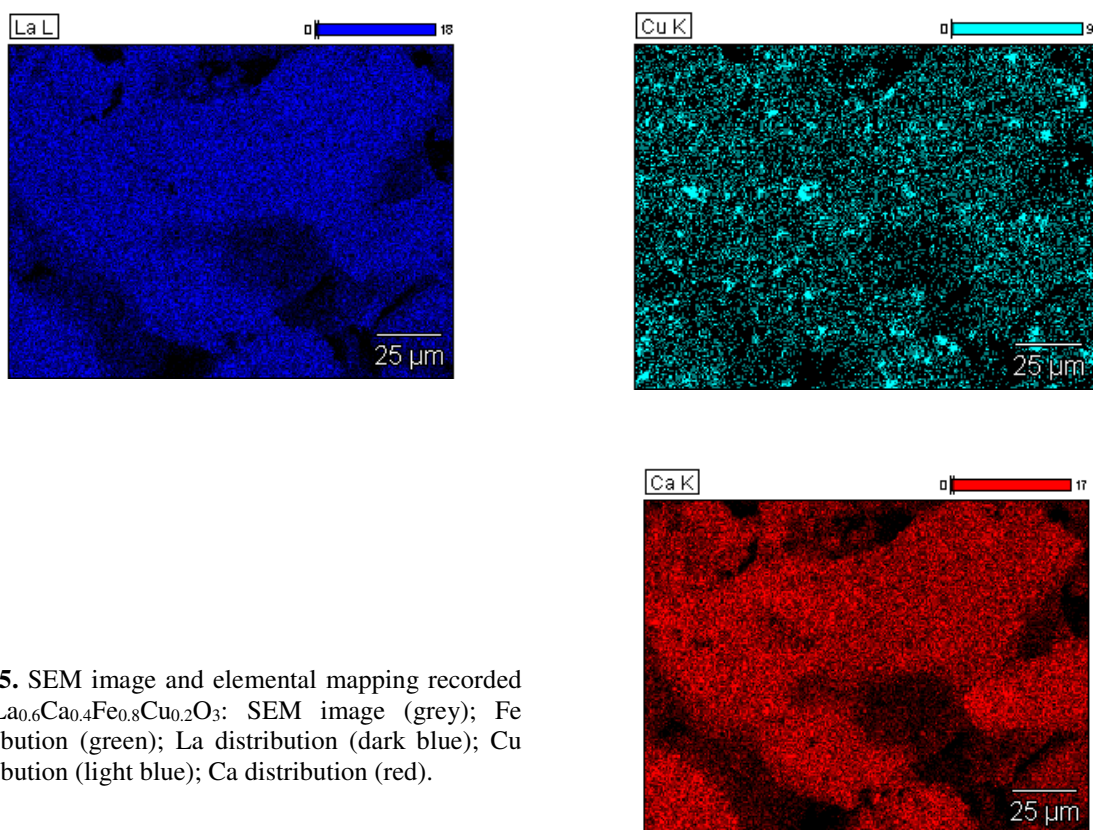


**Fig. 5.** SEM image and elemental mapping recorded on  $\text{La}_{0.6}\text{Ca}_{0.4}\text{Fe}_{0.8}\text{Cu}_{0.2}\text{O}_3$ : SEM image (grey); Fe distribution (green); La distribution (dark blue); Cu distribution (light blue); Ca distribution (red).

**Table 3.** Elemental analysis of dual substituted stoichiometric  $\text{LaFeO}_3$  and La-deficient  $\text{La}_{1-x}\text{FeO}_3$  parent perovskite materials from EDS analysis.

catalyst	Atomic composition (%)						
	La	Ca	Ca/La	Fe	Cu	Cu/Fe	A/B
$\text{LaFeO}_3$	48.6	-	-	51.4	-	-	0.94(1.02)
$\text{La}_{0.7}\text{FeO}_3$	38.0	-	-	62.0	-	-	0.61(0.67)
$\text{La}_{0.7}\text{Fe}_{0.8}\text{Cu}_{0.2}\text{O}_3$	37.1	-	-	50.9	12.0	0.23(0.25)	0.59(0.68)
$\text{La}_{0.6}\text{Ca}_{0.1}\text{Fe}_{0.8}\text{Cu}_{0.2}\text{O}_3$	33.1	6.6	0.2	51.2	9.0	0.18(0.26)	0.66(0.68)
$\text{La}_{0.6}\text{Ca}_{0.2}\text{Fe}_{0.8}\text{Cu}_{0.2}\text{O}_3$	29.0	11.8	0.4	46.6	12.7	0.27(0.26)	0.69(0.79)
$\text{La}_{0.6}\text{Ca}_{0.4}\text{Fe}_{0.8}\text{Cu}_{0.2}\text{O}_3$	27.0	21.9	0.8	43.7	7.4	0.17(0.26)	0.95(0.99)

From elemental analysis in bracket

#### 3.1.4. Bulk Reducibility and oxygen mobility

$\text{H}_2$  consumption profiles vs. temperature are shown in Fig. 6.  $\text{H}_2$ -TPR profiles recorded on the parent  $\text{LaFeO}_3$  and  $\text{La}_{0.7}\text{FeO}_3$  perovskites were included as benchmark in each graph in order to provide clearer comparisons. At first glance, stoichiometric  $\text{LaFeO}_3$  seemed unreducible in the temperature range 100-700°C. Regularity of crystal structure improves the stability of

bulk iron species which can only be partially reduced at higher temperature ( $>750^{\circ}\text{C}$ ). By contrast, the reducibility of  $\text{Fe}^{3+}$  in  $\text{La}_{0.7}\text{FeO}_3$  was tremendously enhanced, featured by two broad peaks in the temperature range  $300\text{-}400^{\circ}\text{C}$  and  $425\text{-}625^{\circ}\text{C}$  ascribed to the reduction of extra-framework hematite species [18]. Fig. 6(A) displayed  $\text{H}_2$  consumption curves for the stoichiometric  $\text{LaFe}_{1-y}\text{Cu}_y\text{O}_3$  perovskites. The contribution below  $300^{\circ}\text{C}$  corresponds to the reduction of oxidic copper species. A small shoulder appears at lower temperature for copper composition  $y = 0.1$  and  $0.2$  assigned to the reduction of more reducible extra-framework copper oxide species and then disappears for  $y = 0.3$  presumably due to the simultaneity of reduction processes and/or less reducible extrameframework  $\text{CuO}$  species due to significant agglomeration process. The reducibility of La-deficient perovskites  $\text{La}_{0.7}\text{Fe}_{1-y}\text{Cu}_y\text{O}_3$  displayed in Fig. 6(C) differs from their stoichiometric counterpart. As seen, a broad  $\text{H}_2$  consumption related to hematite reduction appears for  $y = 0.1$  and attenuates for higher copper concentration. Jointly, the reduction of oxidic copper species shifts to lower temperature and similarly the growth of extra framework species intensifies. As indicated in Table 4, a marked increase of the total  $\text{H}_2$  uptake was recorded on Cu-substituted samples with a rise in copper content, resulting from either the direct introduction of greater amount of copper itself or more stabilized  $\text{Fe}^{4+}$  species confirmed by Mössbauer spectroscopy.

Regarding the reducibility of dual substituted samples in Fig. 6(B), it is worth to note that stoichiometric  $\text{La}_{0.6}\text{Ca}_{0.4}\text{Fe}_{0.8}\text{Cu}_{0.2}\text{O}_3$  sample exhibits a weaker reducibility consistently with previous observations on  $\text{LaFe}_{1-y}\text{Cu}_y\text{O}_3$  emphasizing the beneficial impact of La-deficiency on the reducibility. Ca-substitution on La-deficient  $\text{La}_{0.6}\text{Fe}_{1-y}\text{Cu}_y\text{O}_3$  samples also induces an attenuation of the shoulder at low temperature likely related to a slower aggregation of copper oxide in agreement with SEM-EDS analysis.

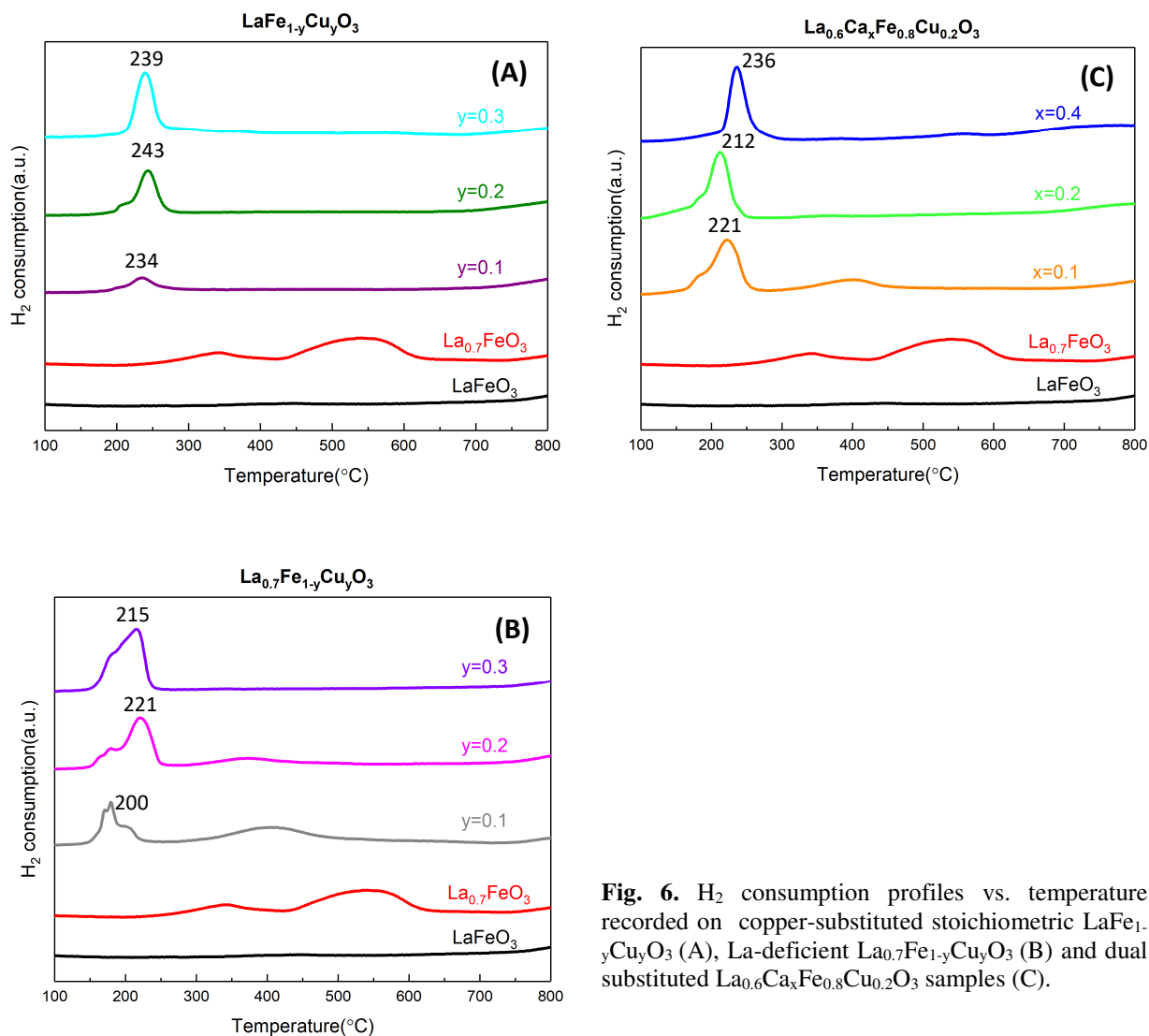


**Fig. 6.** H<sub>2</sub> consumption profiles vs. temperature recorded on copper-substituted stoichiometric LaFe<sub>1-y</sub>Cu<sub>y</sub>O<sub>3</sub> (A), La-deficient La<sub>0.7</sub>Fe<sub>1-y</sub>Cu<sub>y</sub>O<sub>3</sub> (B) and dual substituted La<sub>0.6</sub>Ca<sub>x</sub>Fe<sub>0.8</sub>Cu<sub>0.2</sub>O<sub>3</sub> samples (C).

The mobility of oxygen in the perovskites has been characterized from oxygen-Temperature-Programmed Desorption experiments (O<sub>2</sub>-TPD). Previous investigations reported two different desorption processes corresponding to suprafacial oxygen ( $\alpha$ -oxygen) ascribed to O<sup>-</sup> or O<sub>2</sub><sup>-</sup>. As previously explained [28],  $\alpha$ -oxygen desorption depends on non-stoichiometry and structural defects influenced by the A-cations. The second O<sub>2</sub>-desorption process ( $\beta$ -oxygen), taking place at higher temperature, is more related to the B cations and generally assigned to oxygen lattice species, i.e. O<sup>2-</sup>. Based on this, tentative assignments can be sometimes ambiguous because of the absence of  $\alpha$ -O<sub>2</sub> desorption and/or taking place on a wide

temperature range with significant overlapping with  $\beta$ -desorption [29,30]. By way of illustration, Levasseur and Kaliaguine [29] found  $\alpha$ -O<sub>2</sub> desorption significantly delayed on La<sub>1-x</sub>Ce<sub>x</sub>Co<sub>1-y</sub>Fe<sub>y</sub>O<sub>3</sub> in the range 584-735°C while  $\beta$ -O<sub>2</sub> desorption occurred above 800°C. Some similarities are observable in Fig. 7 on benchmark LaFeO<sub>3</sub> and La<sub>0.7</sub>FeO<sub>3</sub>. On the former system, an unique weak  $\beta$ -O<sub>2</sub> desorption is discernible with an apparent maximum near 850°C whereas an extra  $\alpha$ -O<sub>2</sub> desorption appears on La<sub>0.7</sub>FeO<sub>3</sub> near 705°C. A broad peak below 200°C has been ascribed to surface hydroxyl species and/or physisorbed oxygen species [31]. As this observation is not systematic, then it could be linked to the presence of segregated species. As observed in Table 4, no clear dependency of the amount of oxygen released with the specific surface area appears which would suggest with a predominant intrafacial oxygen desorption.

It is also noticeable that Cu substitution on stoichiometric LaFe<sub>1-y</sub>Cu<sub>y</sub>O<sub>3</sub> compositions has a weak effect on bulk oxygen mobility, only detectable for the highest Cu content. Clearly, La-deficient La<sub>0.7</sub>Fe<sub>1-y</sub>Cu<sub>y</sub>O<sub>3</sub> compositions exhibit improved oxygen mobility with a raise in Cu content corresponding to a sharp increase of the amount of desorbed oxygen (see Fig. 7(B) and Table 4). However,  $\beta$ -O<sub>2</sub> desorption prevails with only a weak shoulder at low temperature emphasizing a weak effect of copper substitution on  $\alpha$ -O<sub>2</sub> desorption suggesting a greater stabilization of anionic vacancies. Besides, compared to stoichiometric LaFe<sub>1-y</sub>Cu<sub>y</sub>O<sub>3</sub> perovskites, La-deficient samples manifest a marked augmentation of desorbed  $\beta$ -oxygen at the same copper substitution degree. O<sub>2</sub>-TPD profiles of dual substituted La<sub>0.6</sub>Ca<sub>x</sub>Fe<sub>0.8</sub>Cu<sub>0.2</sub>O<sub>3</sub> perovskites provide the most significant observations with different behavior toward oxygen desorption. On La-deficient composition, Ca incorporation delays the desorption of intrafacial oxygen whereas the opposite trend characterizes the stoichiometric La<sub>0.6</sub>Ca<sub>0.4</sub>Fe<sub>0.8</sub>Cu<sub>0.2</sub>O<sub>3</sub> composition. Indeed, the desorption takes place at lower temperature in the range 700-820°C (dotted line). In addition, a weak low temperature desorption grows in the range 200-300°C

representative of  $\alpha$ -O<sub>2</sub> desorption process. Such improved oxygen mobility on La<sub>0.6</sub>Ca<sub>0.4</sub>Fe<sub>0.8</sub>Cu<sub>0.2</sub>O<sub>3</sub> could be related to an alteration of the structural stability with strong lattice distortions induced by calcium doping observed from XRD and Mössbauer spectroscopy but also the stabilization of Fe<sup>4+</sup> species which could correspond to a weakening of the Fe/Cu-O bond corresponding to a lower energy formation of anionic vacancies. Hence, the weaker oxygen mobility of the La-deficient perovskites could be related to less structural disorders in comparison to the stoichiometric specimen exhibiting a greater stabilization of cationic iron and copper species in distorted octahedrons of the perovskite lattice.

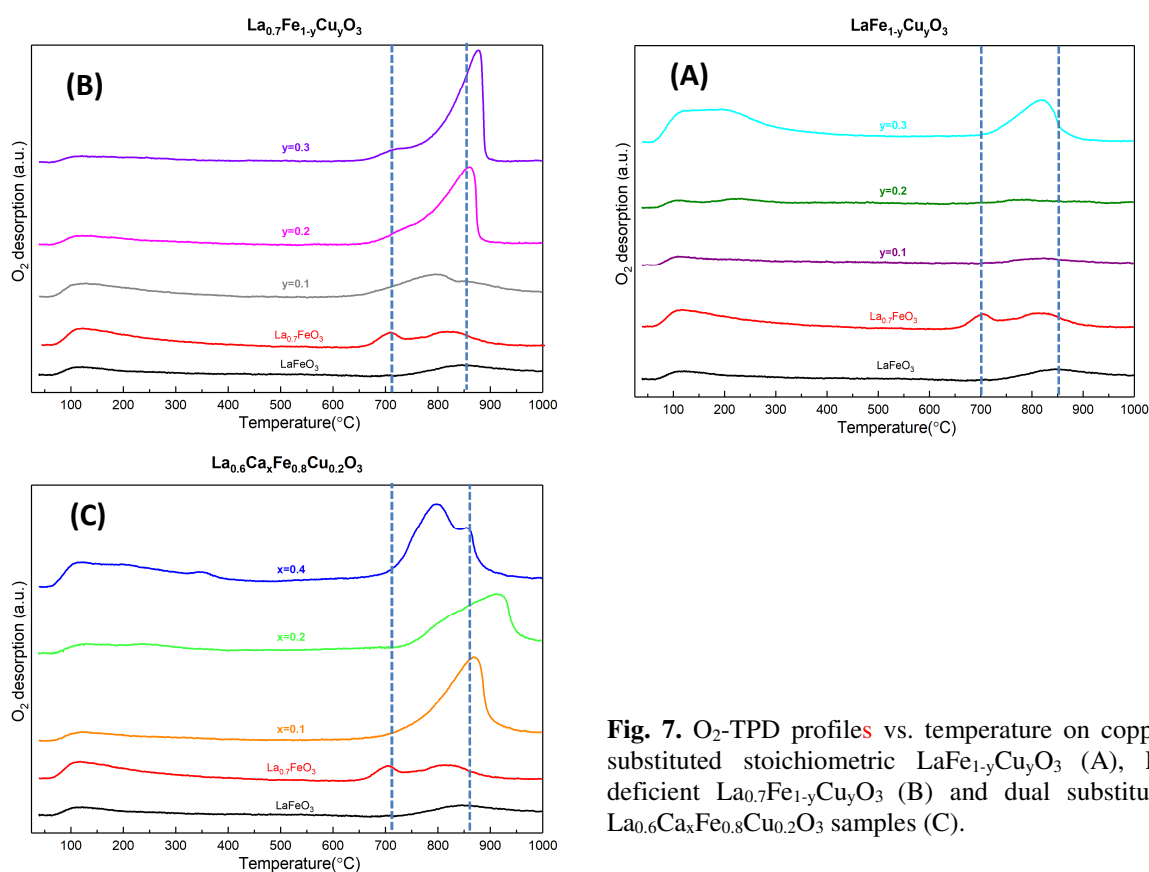


**Fig. 7.** O<sub>2</sub>-TPD profiles vs. temperature on copper-substituted stoichiometric LaFe<sub>1-y</sub>Cu<sub>y</sub>O<sub>3</sub> (A), La-deficient La<sub>0.7</sub>Fe<sub>1-y</sub>Cu<sub>y</sub>O<sub>3</sub> (B) and dual substituted La<sub>0.6</sub>Ca<sub>x</sub>Fe<sub>0.8</sub>Cu<sub>0.2</sub>O<sub>3</sub> samples (C).

**Table 4.** Impact of copper and calcium substitution on the textural properties, reducibility and oxygen mobility of parent stoichiometric LaFeO<sub>3</sub> and La-deficient La<sub>0.7</sub>FeO<sub>3</sub> perovskites

Catalyst	Porosity measurements			H <sub>2</sub> -TPR measurements		Amount O <sub>2</sub> desorbed (mmol g <sup>-1</sup> ) <sup>b</sup>
	S <sub>BET</sub> (m <sup>2</sup> /g)	S <sub>th</sub> (m <sup>2</sup> /g) <sup>a</sup>	S <sub>th</sub> /S <sub>BET</sub>	H <sub>2</sub> uptake (mmol g <sup>-1</sup> )	H/Cu+Fe	
LaFeO <sub>3</sub>	15.5	30.8	2.0	-	-	0.03
La <sub>0.7</sub> FeO <sub>3</sub>	35.5	41.7	1.2	1.45	0.58	0.12
LaFe <sub>0.9</sub> Cu <sub>0.1</sub> O <sub>3</sub>	19.2	29.0	1.5	0.29	0.14	0.03
LaFe <sub>0.8</sub> Cu <sub>0.2</sub> O <sub>3</sub>	15.3	26.9	1.8	0.72	0.35	0.03
LaFe <sub>0.7</sub> Cu <sub>0.3</sub> O <sub>3</sub>	26.2	35.2	1.3	1.15	0.56	0.14
La <sub>0.7</sub> Fe <sub>0.9</sub> Cu <sub>0.1</sub> O <sub>3</sub>	32.2	37.2	1.2	1.26	0.51	0.16
La <sub>0.7</sub> Fe <sub>0.8</sub> Cu <sub>0.2</sub> O <sub>3</sub>	23.2	31.6	1.4	1.27	0.52	0.34
La <sub>0.7</sub> Fe <sub>0.7</sub> Cu <sub>0.3</sub> O <sub>3</sub>	15.4	21.4	1.4	1.41	0.57	0.42
La <sub>0.6</sub> Ca <sub>0.1</sub> Fe <sub>0.8</sub> Cu <sub>0.2</sub> O <sub>3</sub>	22.1	27.8	1.3	1.44	0.56	0.38
La <sub>0.6</sub> Ca <sub>0.2</sub> Fe <sub>0.8</sub> Cu <sub>0.2</sub> O <sub>3</sub>	21.3	29.8	1.4	1.10	0.43	0.35
La <sub>0.6</sub> Ca <sub>0.4</sub> Fe <sub>0.8</sub> Cu <sub>0.2</sub> O <sub>3</sub>	32.4	37.1	1.2	1.07	0.44	0.44

<sup>a</sup> S<sub>th</sub> = 6×10<sup>3</sup>/ρ<sub>perovskite</sub> d<sub>cryst</sub>.

<sup>b</sup> Total amount of desorbed oxygen in the temperature range 600-1000°C

### 3.2. Surface properties

Textural properties of the prepared perovskites were investigated from nitrogen physisorption. The corresponding isotherms and pore size distributions are reported in Fig. S5 in SI. The values of specific surface area are collected in Table 4. The calcined perovskites at 600°C exhibit low specific surface area and a weak porosity. It is worthwhile to note that La-deficiency induces significant improvements on  $S_{\text{BET}}$ . On the other hand, a rise in copper content leads to the opposite trend significantly marked on  $\text{La}_{0.7}\text{Fe}_{0.7}\text{Cu}_{0.3}\text{O}_3$ . Theoretical surface areas have been estimated from the average crystallite size calculated in Table 1 and compared to the  $S_{\text{BET}}$  values. As seen, the numerical values for the ratio  $S_{\text{th}}/S_{\text{BET}}$  keep almost constant which denotes that changes in the specific surface area are essentially related to crystallite growth.

X-ray photoelectron spectroscopic analysis was implemented to analyze the surface on a depth in the range 5-10 nm. For bulk catalysts this resolution can provide information on the oxidation state and the elemental composition representative of the outermost layer. Binding Energy (B.E.) values have been obtained from the characteristic La 3d, Ca 2p, Fe 2p, Cu 2p and O 1s core levels with C 1s used as reference at 284.8 eV. XPS photopeaks are reported in Figs. S6-S9 in SI. The corresponding B.E. values are collected and compared in Table 5. They underline a stabilization of  $\text{La}^{3+}$  and  $\text{Ca}^{2+}$  on all dual-substituted samples. The Fe 2p photopeak is usually characterized by the presence of a shake-up satellite structure near 719.0 eV with only slight deviations on the B.E. of Fe 2p<sub>3/2</sub> photopeak which agrees with the predominance of  $\text{Fe}^{3+}$  species. On the other hand, changes in spectral features are observable on the Cu 2p<sub>3/2</sub> photopeak with B.E. value varying in the range 932.8 and 934.4 eV. A shake-up satellite structure also appears the range 939-950 eV characteristic of  $\text{Cu}^{2+}$ . Reduced and oxidized copper species are currently reported near 932.6 and 934.2 eV [32,33]. Accordingly, the Cu 2p core level near 934.0 eV, with a more intense shake-up satellite structure, reflects a

greater stabilization of  $\text{Cu}^{2+}$  especially on Ca-doped samples. The lower B.E. values on  $\text{LaFe}_{1-y}\text{Cu}_y\text{O}_3$ , associated to an attenuation of the shake-up structure, emphasize a stabilization of oxidic copper in a lower valent state. Such explanation seems in rather good agreement with a previous investigation [34]. The origin of the formation of copper reduced species has been reported elsewhere from XPS analysis [35,36] and has been assigned to more reducible extra-framework  $\text{Cu}^{2+}$  species likely stabilized at the surface as CuO compared to  $\text{Cu}^{2+}$  in octahedral coordination inside the perovskite lattice. Hence, under X-ray beam irradiation, these less stable CuO species would decompose to Cu(I) and  $\text{Cu}^0$  [35]. The semi-quantitative analysis summarized in Table 5 reveals usual surface La enrichment on stoichiometric compositions which attenuates on La-deficient counterparts and even tends to disappear on  $\text{La}_{0.7}\text{FeO}_3$  and on dual-substituted  $\text{La}_{0.6}\text{Ca}_x\text{Fe}_{1-y}\text{Cu}_y\text{O}_3$  perovskite compositions. The surface La/Ca ratio does not deviate significantly compared to values obtained from elemental analysis. On the other hand, significant fluctuations arise on the surface Cu/Fe ratio. The values deduced from surface analysis are usually lower than those calculated from elemental analysis. Nevertheless, significant deviations on surface Cu/Fe ratio appear on  $\text{La}_{0.7}\text{Fe}_{1-y}\text{Cu}_y\text{O}_3$  related to surface Cu enrichment with a rise in Cu content. In contrast, calcium doping on dual substituted compositions would slightly slow this process. This tendency seems consistent with the higher B.E. corresponding to less reducible  $\text{Cu}^{2+}$  species keeping their initial coordination inside the perovskite framework.

**Table 5.** XPS features on dual substituted stoichiometric LaFeO<sub>3</sub> and La-deficient La<sub>1-x</sub>FeO<sub>3</sub> parent perovskite materials.

Catalyst	Binding energy (eV)							Semi-quantitative analysis			
	La 3d	Ca 2p	Fe 2p	Cu 2p	O 1s (O <sub>ads</sub> )	O 1s (O <sub>lattice</sub> )	C 1s	Ca/La	Cu/Fe	A/B	O <sub>ads</sub> /O <sub>lattice</sub>
LaFeO <sub>3</sub>	833.8	-	710.2	-	531.1	529.2	289.0	-	-	1.34(1.02)	1.28
La <sub>0.7</sub> FeO <sub>3</sub>	834.2	-	710.9	-	531.2	529.7	289.1	-	-	0.48(0.67)	1.61
LaFe <sub>0.9</sub> Cu <sub>0.1</sub> O <sub>3</sub>	833.8	-	710.3	932.9	531.5	529.3	289.3	-	0.13(0.11)	1.18(0.99)	0.96
LaFe <sub>0.8</sub> Cu <sub>0.2</sub> O <sub>3</sub>	833.6	-	709.8	932.8	531.6	529.2	289.3	-	0.22(0.25)	1.21(0.97)	1.22
LaFe <sub>0.7</sub> Cu <sub>0.3</sub> O <sub>3</sub>	833.7	-	709.9	932.9	531.3	529.0	289.2	-	0.12(0.44)	1.43(0.97)	1.14
La <sub>0.7</sub> Fe <sub>0.9</sub> Cu <sub>0.1</sub> O <sub>3</sub>	833.8	-	710.2	933.7	531.4	529.4	288.7	-	0.15(0.11)	0.45(0.67)	0.80
La <sub>0.7</sub> Fe <sub>0.8</sub> Cu <sub>0.2</sub> O <sub>3</sub>	833.7	-	710.6	933.1	531.3	529.2	288.9	-	0.18(0.26)	0.52(0.68)	0.75
La <sub>0.7</sub> Fe <sub>0.7</sub> Cu <sub>0.3</sub> O <sub>3</sub>	833.8	-	710.0	934.0	531.5	529.3	288.9	-	0.29(0.44)	0.75(0.69)	0.67
La <sub>0.6</sub> Ca <sub>0.1</sub> Fe <sub>0.8</sub> Cu <sub>0.2</sub> O <sub>3</sub>	833.4	346.5	710.2	934.1	531.2	529.0	288.9	0.17(0.17)	0.16(0.26)	0.55(0.68)	0.78
La <sub>0.6</sub> Ca <sub>0.2</sub> Fe <sub>0.8</sub> Cu <sub>0.2</sub> O <sub>3</sub>	833.3	346.2	709.9	934.4	531.3	529.0	288.9	0.32(0.33)	0.15(0.26)	0.76(0.79)	0.88
La <sub>0.6</sub> Ca <sub>0.4</sub> Fe <sub>0.8</sub> Cu <sub>0.2</sub> O <sub>3</sub>	833.5	346.6	709.9	934.1	531.4	529.0	289.3	0.55(0.69)	0.08(0.26)	0.98(0.99)	1.05

Elemental composition in bracket

### 3.3. Evaluation of Three-Way-Catalytic properties

As depicted in the experimental section, four successive temperature cycles, from 100 °C to 550 °C, were performed according to the following sequence : Stoichiometry (STO1)/Lean/Rich/Stoichiometry (STO2). The corresponding TPR conversion curves are reported in Figs. S10 and S11 in SI. Let us keep in mind that STO1 curves were recorded on samples pre-heated in air at 600°C and then activated for 2 h in the reaction mixture at the same temperature. The comparison of catalytic performances from initial (STO1) and final (STO2) TPR experiments is useful to check changes in catalytic performances due to possible alterations of the catalyst surface in terms of composition and valence state of active elements, induced by successive lean/rich cycles.

Oxidative properties have been preferentially examined through CO, propene and propane conversion in agreement with inlet gas compositions reported in Table S1 (SI). It was found that La-deficient  $\text{La}_{0.7}\text{Fe}_{1-y}\text{Cu}_y\text{O}_3$  catalyst promotes CO oxidation but slight deactivation occurs at high copper loading. At a first glance, a better stability is observed on  $\text{La}_{0.6}\text{Ca}_x\text{Fe}_{0.8}\text{Cu}_{0.2}\text{O}_3$  with quasi-superimposed conversion curves emphasizing the beneficial effect of calcium. For propene oxidation, the most prominent change was observed on  $\text{La}_{0.6}\text{Ca}_{0.2}\text{Fe}_{0.8}\text{Cu}_{0.2}\text{O}_3$  giving rise to a sharp increase in propene conversion accentuating during STO2 experiment. At first glance, one can hypothesize that a slower copper segregation corresponding to an improved stabilization of isolated  $\text{Cu}^{2+}$  species in octahedral coordination inside the perovskite framework, as illustrated from physicochemical characterization, would be responsible of improved performances on  $\text{La}_{0.6}\text{Ca}_{0.2}\text{Fe}_{0.8}\text{Cu}_{0.2}\text{O}_3$  in terms of activity and stability.

NO conversion profiles vs. temperature are reported in Fig. S12 in SI. Clearly, perovskite itself is unable to convert  $\text{NO}_x$  to nitrogen, except in rich conditions. As can be seen, the best

compromise is observed on dual substituted  $\text{La}_{0.6}\text{Ca}_{0.1}\text{Fe}_{0.8}\text{Cu}_{0.2}\text{O}_3$  samples combining A-deficiency and copper substitution. Mössbauer spectroscopy clearly shows a better structural stabilization induced by A-deficiency which could be a guideline for developing more stable systems in critical temperature ranges compared to stoichiometric perovskite compositions especially for stabilizing copper dispersion. However, an important parameter is likely related to a low density of copper sites available for NO reduction. Interesting observations have been reported on  $\text{LaCo}_{1-x}\text{Cu}_x\text{O}_3$  [5] and on  $\text{CuO}/\text{LaCoO}_3$  nanocomposites [6]. They emphasize the beneficial impact of well-dispersed CuO species at the surface. These investigations also pointed out the importance to preserve their dispersion in critical operating TWC conditions thanks to an innovative Ammonium-Driving Deposition precipitation which combines high dispersion and high density of active sites [6]. Nevertheless, all these observations stress the importance of introducing a low concentration of precious metal for improving significantly NO conversion at lower temperature [35].

### 3.3.2. Kinetic analysis

In order to get more insights into the role played by copper and calcium, kinetic analysis has been focused on CO and propene oxidation from transient experiments in stoichiometric conditions, with the aim to have a more detailed analysis of the role of Cu and Ca substitutions and if La-deficient and stoichiometric composition are affected similarly. The mass balance for a plug flow reactor has been considered in these calculations and a first order kinetics has been assumed in agreement with earlier investigations [35,37].

Specific and normalized rates, expressed per  $\text{m}^2$ , respectively labeled  $r_{\text{spec.}}$  and  $r_{\text{norm.}}$ , as well as pre-exponential factor and apparent activation energy of the rate constant  $k$  for CO and propene oxidation have been estimated at  $250^\circ\text{C}$  and  $375^\circ\text{C}$  respectively. The estimates from conversion recorded during the first cycle (STO1) and the final cycle (STO2) are collected

and compared in Tables 6 and 7. The order of magnitude of  $E_{app}$  values shows that external mass transfer diffusion phenomena should not be prevalent. As these materials do not exhibit significant porosity, then internal diffusion phenomena should not occur significantly in our operating conditions. We also verified the boundary conditions given by the Weiss-Prater criterion in Eq. (S4) in SI, for conversions lower than 40%.

### *STO1 experiments*

Regarding STO1 experiments, it is interesting to note that different behaviors for CO oxidation appear distinctly at 250°C. Indeed, rate measurements show that copper substitution jointly with lanthanum deficiency induces a sharp increase of the specific and normalized rates compared to the benchmark  $\text{LaFeO}_3$  and  $\text{La}_{0.7}\text{FeO}_3$  with an optimum on  $\text{La}_{0.7}\text{Fe}_{0.8}\text{Cu}_{0.2}\text{O}_3$ . Such an observation is correlated to a significant lessening of the apparent activation energy from 121 and 108 to 72  $\text{kJ mol}^{-1}$  respectively. Such rate enhancement is less pronounced on stoichiometric  $\text{LaFe}_{1-y}\text{Cu}_y\text{O}_3$  samples except at the highest Cu content corresponding to  $y = 0.3$ . Subsequent substitution of La by Ca has a slight detrimental effect on the rates in comparison with  $\text{La}_{0.7}\text{Fe}_{0.8}\text{Cu}_{0.2}\text{O}_3$ . A weak calcium dependency of the specific and normalized rate and apparent activation energy is also discernible which does not reveal the existence of optimal composition as previously observed on  $\text{La}_{0.7}\text{Fe}_{1-y}\text{Cu}_y\text{O}_3$ .

Now, regarding propene oxidation, it seems obvious that copper substitution on  $\text{La}_{0.7}\text{FeO}_3$  and  $\text{LaFeO}_3$  induces similar tendencies than those observed for CO oxidation but in weaker extent. A slight detrimental effect is even observed on the stoichiometric  $\text{LaFe}_{1-y}\text{Cu}_y\text{O}_3$  samples for  $y \leq 0.2$  corresponding to an increase in  $E_{app}$  partly compensated by an increase of the pre-exponential factor. Surprisingly, an opposite behavior is distinguishable with a positive effect of calcium substitution on the specific rate value of  $\text{La}_{0.6}\text{Ca}_{0.2}\text{Fe}_{0.8}\text{Cu}_{0.2}\text{O}_3$  accompanied with a lessening of  $E_{app}$ . Nevertheless, this effect seems restricted to La-

deficient samples. As observed, calcium substitution leads to a sharp loss of catalytic activity on stoichiometric  $\text{La}_{0.6}\text{Ca}_{0.4}\text{Fe}_{0.8}\text{Cu}_{0.2}\text{O}_3$  perovskite jointly with a sharp increase in  $E_{\text{app}}$ . The evolution observed on the pre-exponential factor values in Tables 5 and 6 seems to be independent of the specific surface area.

### *STO2 experiments*

The comparison of kinetic data from STO1 experiment provides general trends which show a relative stability with no strong deactivation based on the comparison of specific and normalized rate. However, a closer examination reveals distinct behavior for CO oxidation at low and high copper content on La-deficient  $\text{La}_{0.7}\text{Fe}_{1-y}\text{Cu}_y\text{O}_3$  and stoichiometric  $\text{LaFe}_{1-y}\text{Cu}_y\text{O}_3$  samples. As aforementioned, optimal composition has been observed on the series  $\text{La}_{0.7}\text{Fe}_{1-y}\text{Cu}_y\text{O}_3$  for  $y = 0.2$  from STO1 experiments which is no longer observed by examining the specific rate values, but still persists from the normalized rates. Indeed, for  $y \leq 0.2$ , a slight rate improvement is observed whereas a stabilization or weak loss of activity is discernible for  $y > 0.2$  ( $y = 0.3$ ). Let us now examine the stoichiometric series  $\text{LaFe}_{1-y}\text{Cu}_y\text{O}_3$  which did not reveal initially optimal copper composition. By examining STO2 rate values, the appearance of an optimal composition is remarkable for  $y = 0.2$ . Similarly to the STO1 series, the pre-exponential values of the rate constants still remain independent of the specific surface area. Such comparison would suggest that the density of active sites would not be related to the extent of the catalyst surface. The copper dispersion/aggregation processes would play an important role in determining the density of active copper sites at the surface for CO oxidation. The aggregation process would accelerate for the highest Cu composition leading to a detrimental effect on the reaction rate. Hence, despite such process would be slower on stoichiometric compositions, it seems obvious that lean/rich exposure facilitates copper

extraction/surface segregation processes. A strong acceleration on La-deficient materials induces deactivation.

The evolutions observed after Ca substitution also provide interesting information because in that case a lowering of specific and normalized rate is noticeable in comparison to  $\text{La}_{0.7}\text{Fe}_{1-y}\text{Cu}_y\text{O}_3$  highlighting a slight detrimental effect of calcium assigned to a slower segregation minimizing the density of active Cu sites. As previously mentioned, the impact of calcium differs for propene oxidation. An increase in the specific and intrinsic rates on  $\text{La}_{0.6}\text{Ca}_{0.2}\text{Fe}_{0.8}\text{Cu}_{0.2}\text{O}_3$  is still remarkable and accentuate compared to rates measured in STO1 conditions. Similarly, the opposite behavior of calcium on the stoichiometric composition is noticeable with a sharp deactivation.

**Table 6.** Rate and kinetic parameters related to CO oxidation on dual substituted stoichiometric LaFeO<sub>3</sub> and La-deficient La<sub>1-x</sub>FeO<sub>3</sub> parent perovskite materials

Catalyst	S <sub>BET</sub> (m <sup>2</sup> g <sup>-1</sup> )	STO1				STO2			
		r <sub>spec.</sub> <sup>a</sup> (mol s <sup>-1</sup> g <sup>-1</sup> )	r <sub>nom.</sub> <sup>b</sup> (mol s <sup>-1</sup> m <sup>-2</sup> )	A <sup>c</sup> (m <sup>3</sup> s <sup>-1</sup> g <sup>-1</sup> )	E <sub>app</sub> <sup>c</sup> (kJ mol <sup>-1</sup> )	r <sub>spec.</sub> <sup>a</sup> (mol s <sup>-1</sup> g <sup>-1</sup> )	r <sub>nom.</sub> <sup>b</sup> (mol s <sup>-1</sup> m <sup>-2</sup> )	A <sup>c</sup> (m <sup>3</sup> s <sup>-1</sup> g <sup>-1</sup> )	E <sub>app</sub> <sup>c</sup> (kJ mol <sup>-1</sup> )
LaFeO <sub>3</sub>	15.5	0.1×10 <sup>-8</sup>	0.5×10 <sup>-10</sup>	3.6×10 <sup>3</sup>	121	0.01×10 <sup>-8</sup>	0.6×10 <sup>-10</sup>	2.9×10 <sup>3</sup>	162
La <sub>0.7</sub> FeO <sub>3</sub>	35.5	1.6×10 <sup>-8</sup>	4.5×10 <sup>-10</sup>	3.3×10 <sup>3</sup>	108	0.6×10 <sup>-8</sup>	1.7×10 <sup>-10</sup>	4.3×10 <sup>4</sup>	123
LaFe <sub>0.9</sub> Cu <sub>0.1</sub> O <sub>3</sub>	19.2	1.7×10 <sup>-8</sup>	8.8×10 <sup>-10</sup>	3.6×10 <sup>11</sup>	188	5.6×10 <sup>-8</sup>	29.1×10 <sup>-10</sup>	7.1×10 <sup>8</sup>	156
LaFe <sub>0.8</sub> Cu <sub>0.2</sub> O <sub>3</sub>	15.3	1.6×10 <sup>-8</sup>	10.3×10 <sup>-10</sup>	4.5×10 <sup>10</sup>	179	16.2×10 <sup>-8</sup>	106×10 <sup>-10</sup>	5.1×10 <sup>5</sup>	120
LaFe <sub>0.7</sub> Cu <sub>0.3</sub> O <sub>3</sub>	26.2	39.8×10 <sup>-8</sup>	152×10 <sup>-10</sup>	14	70	13.5×10 <sup>-8</sup>	51.4×10 <sup>-10</sup>	5.9×10 <sup>7</sup>	141
La <sub>0.7</sub> Fe <sub>0.9</sub> Cu <sub>0.1</sub> O <sub>3</sub>	32.2	20.9×10 <sup>-8</sup>	64.8×10 <sup>-10</sup>	150	83	49.7×10 <sup>-8</sup>	154×10 <sup>-10</sup>	290	82
La <sub>0.7</sub> Fe <sub>0.8</sub> Cu <sub>0.2</sub> O <sub>3</sub>	23.2	80.2×10 <sup>-8</sup>	346×10 <sup>-10</sup>	53	72	45.1×10 <sup>-8</sup>	194×10 <sup>-10</sup>	2.2×10 <sup>3</sup>	91
La <sub>0.7</sub> Fe <sub>0.7</sub> Cu <sub>0.3</sub> O <sub>3</sub>	15.4	18.3×10 <sup>-8</sup>	119×10 <sup>-10</sup>	5.5×10 <sup>3</sup>	99	22.0×10 <sup>-8</sup>	143×10 <sup>-10</sup>	170	83
La <sub>0.6</sub> Ca <sub>0.1</sub> Fe <sub>0.8</sub> Cu <sub>0.2</sub> O <sub>3</sub>	22.1	39.6×10 <sup>-8</sup>	179×10 <sup>-10</sup>	700	87	18.1×10 <sup>-8</sup>	81.8×10 <sup>-10</sup>	5.2×10 <sup>5</sup>	119
La <sub>0.6</sub> Ca <sub>0.2</sub> Fe <sub>0.8</sub> Cu <sub>0.2</sub> O <sub>3</sub>	21.3	39.4×10 <sup>-8</sup>	185×10 <sup>-10</sup>	340	84	23.6×10 <sup>-8</sup>	111×10 <sup>-10</sup>	1.7×10 <sup>3</sup>	93
La <sub>0.6</sub> Ca <sub>0.4</sub> Fe <sub>0.8</sub> Cu <sub>0.2</sub> O <sub>3</sub>	32.4	39.8×10 <sup>-8</sup>	123×10 <sup>-10</sup>	110	80	25.8×10 <sup>-8</sup>	79.7×10 <sup>-10</sup>	0.9	60

<sup>a</sup> specific rate calculated at T = 250°C

<sup>b</sup> normalized rate calculated at T = 250°C

<sup>c</sup> A pre-exponential factor and E<sub>app</sub> apparent activation energy in agreement with k = A exp(-E<sub>app</sub>/RT)

**Table 7.** Rate and kinetic parameters related to C<sub>3</sub>H<sub>6</sub> oxidation on dual substituted stoichiometric LaFeO<sub>3</sub> and La-deficient La<sub>1-x</sub>FeO<sub>3</sub> parent perovskite materials

Catalyst	S <sub>BET</sub> (m <sup>2</sup> g <sup>-1</sup> )	STO1				STO2			
		r <sub>spec.</sub> <sup>a</sup> (mol s <sup>-1</sup> g <sup>-1</sup> )	r <sub>norm.</sub> <sup>b</sup> (mol s <sup>-1</sup> m <sup>-2</sup> )	A <sup>c</sup> (m <sup>3</sup> s <sup>-1</sup> g <sup>-1</sup> )	E <sub>app</sub> <sup>c</sup> (kJ mol <sup>-1</sup> )	r <sub>spec.</sub> <sup>a</sup> (mol s <sup>-1</sup> g <sup>-1</sup> ) <sup>a</sup>	r <sub>norm.</sub> <sup>b</sup> (mol s <sup>-1</sup> m <sup>-2</sup> ) <sup>a</sup>	A <sup>c</sup> (m <sup>3</sup> s <sup>-1</sup> g <sup>-1</sup> )	E <sub>app</sub> <sup>c</sup> (kJ mol <sup>-1</sup> )
LaFeO <sub>3</sub>	15.5	1.1×10 <sup>-8</sup>	6.9×10 <sup>-10</sup>	7.1×10 <sup>3</sup>	125	0.8×10 <sup>-8</sup>	5.3×10 <sup>-10</sup>	1.2×10 <sup>4</sup>	130
La <sub>0.7</sub> FeO <sub>3</sub>	35.5	1.7×10 <sup>-8</sup>	4.9×10 <sup>-10</sup>	7.5×10 <sup>3</sup>	123	1.3×10 <sup>-8</sup>	3.6×10 <sup>-10</sup>	4.5×10 <sup>4</sup>	134
LaFe <sub>0.9</sub> Cu <sub>0.1</sub> O <sub>3</sub>	19.2	0.01×10 <sup>-8</sup>	0.4×10 <sup>-10</sup>	1.3×10 <sup>11</sup>	229	0.3×10 <sup>-8</sup>	1.4×10 <sup>-10</sup>	7.1×10 <sup>6</sup>	170
LaFe <sub>0.8</sub> Cu <sub>0.2</sub> O <sub>3</sub>	15.3	0.3×10 <sup>-8</sup>	1.9×10 <sup>-10</sup>	1.1×10 <sup>7</sup>	172	3.3×10 <sup>-8</sup>	21.7×10 <sup>-10</sup>	458	160
LaFe <sub>0.7</sub> Cu <sub>0.3</sub> O <sub>3</sub>	26.2	4.4×10 <sup>-8</sup>	16.8×10 <sup>-10</sup>	4.6×10 <sup>4</sup>	127	5.1×10 <sup>-8</sup>	19.4×10 <sup>-10</sup>	1.1×10 <sup>5</sup>	130
La <sub>0.7</sub> Fe <sub>0.9</sub> Cu <sub>0.1</sub> O <sub>3</sub>	32.2	4.5×10 <sup>-8</sup>	14.0×10 <sup>-10</sup>	2.5×10 <sup>6</sup>	148	10.2×10 <sup>-8</sup>	31.7×10 <sup>-10</sup>	707	98
La <sub>0.7</sub> Fe <sub>0.8</sub> Cu <sub>0.2</sub> O <sub>3</sub>	23.2	4.9×10 <sup>-8</sup>	21.3×10 <sup>-10</sup>	3.4×10 <sup>5</sup>	136	11.3×10 <sup>-8</sup>	48.9×10 <sup>-10</sup>	5.0×10 <sup>4</sup>	121
La <sub>0.7</sub> Fe <sub>0.7</sub> Cu <sub>0.3</sub> O <sub>3</sub>	15.4	1.1×10 <sup>-8</sup>	7.12×10 <sup>-10</sup>	6.6×10 <sup>3</sup>	125	4.1×10 <sup>-8</sup>	26.9×10 <sup>-10</sup>	179	97
La <sub>0.6</sub> Ca <sub>0.1</sub> Fe <sub>0.8</sub> Cu <sub>0.2</sub> O <sub>3</sub>	22.1	3.0×10 <sup>-8</sup>	13.5×10 <sup>-10</sup>	24	89	17.0×10 <sup>-8</sup>	77.1×10 <sup>-10</sup>	1.6×10 <sup>4</sup>	114
La <sub>0.6</sub> Ca <sub>0.2</sub> Fe <sub>0.8</sub> Cu <sub>0.2</sub> O <sub>3</sub>	21.3	12.0×10 <sup>-8</sup>	55.8×10 <sup>-10</sup>	165	88	32.5×10 <sup>-8</sup>	152×10 <sup>-10</sup>	5.8×10 <sup>10</sup>	84
La <sub>0.6</sub> Ca <sub>0.4</sub> Fe <sub>0.8</sub> Cu <sub>0.2</sub> O <sub>3</sub>	32.4	0.5×10 <sup>-8</sup>	1.5×10 <sup>-10</sup>	9.8×10 <sup>5</sup>	156	1.1×10 <sup>-8</sup>	3.3×10 <sup>-10</sup>	2.0×10 <sup>4</sup>	116

<sup>a</sup> specific rate calculated at T = 375°C

<sup>b</sup> normalized rate calculated at T = 375°C

<sup>c</sup> A pre-exponential factor and E<sub>app</sub> apparent activation energy in agreement with k = Aexp(-E<sub>app</sub>/RT)

#### 4. Discussion

The establishment of structure-reactivity relationships is not trivial by analyzing catalytic measurements showing sometimes opposite behaviors after Cu and Ca substitutions on La-deficient  $\text{La}_{0.7}\text{FeO}_3$  and stoichiometric  $\text{LaFeO}_3$  perovskites. It is remarkable that trends observed for CO oxidation can be no longer observed for hydrocarbon conversion, which would suggest that key elementary steps for these two reactions could not refer to the same catalytic functionality. Previously, Voorhoeve et al. [38] suggested for oxidation reactions on perovskite two distinct reaction mechanisms. The first one involves changes in the oxidation state of the active elements, periodically restored at the end of continuous cycles and associated to lattice oxygen of the perovskite as active species. The second one requires optimal symmetry and energy of atomic orbitals to be conducive for the reaction and would involve adsorbed oxygen species from the gas phase. Both mechanisms conventionally labeled intrafacial and suprafacial prevail at high and low temperature respectively.

A key point provided by our observations is first related to single and dual substitutions which induce strong structural distortions, changes in the oxidation state of B-site and modification in the oxygen mobility. More complex features are undoubtedly related to the coexistence of different oxidic copper species in octahedral coordination inside the perovskite lattice and more reducible extraframework CuO species with catalytic properties controlled by their dispersion. Indeed, their aggregation observed at increasing Cu loading induces a loss of catalytic properties on  $\text{La}_{0.7}\text{Fe}_{1-y}\text{Cu}_y\text{O}_3$ . Calcium substitution could be a strategy to monitor the density and the dispersion of these extraframework Cu active species, but this peculiarity is restricted to La-deficient compositions.

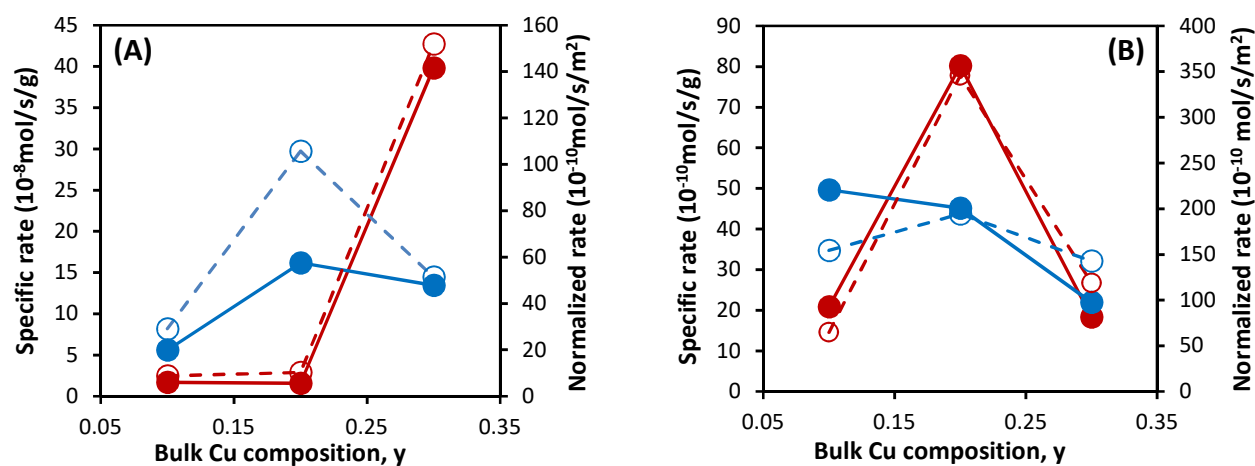
Bulk characterization showed that the replacement of trivalent ( $\text{La}^{3+}$ ) by divalent  $\text{Ca}^{2+}$  cations can create significant electronic imbalances and structural distortions. Based on this, charge

compensation can be obtained by changes in the valence state of B-sites or the creation of oxygen vacancies. In principle, the appearance of anionic vacancies should be accompanied to a greater oxygen adsorption which can potentially lead to gain in catalytic activity. Starting from single iron substitution by copper, the changes in ionic radius, i.e.  $r(\text{Cu}^{2+}) = 0.72 \text{ \AA}$  versus  $r(\text{Fe}^{3+}) = 0.64 \text{ \AA}$ , should induce an expansion of the cell volume. In practice, Rietveld refinement calculations did not reveal significant changes in the cell volume on  $\text{LaFe}_{1-y}\text{Cu}_y\text{O}_3$  and  $\text{La}_{0.7}\text{Fe}_{1-y}\text{Cu}_y\text{O}_3$  compositions. Indeed, this expansion effect could be counterbalanced by contraction effects due to the creation of oxygen vacancies or the stabilization of  $\text{Fe}^{4+}$  corresponding to a lower ionic radius of  $0.585 \text{ \AA}$  [39]. The presence of  $\text{Fe}^{4+}$  has not been characterized from Mössbauer spectroscopy on La-deficient perovskite compositions. They only appear on stoichiometric compositions  $\text{LaFeO}_3$ ,  $\text{LaFe}_{0.8}\text{Cu}_{0.2}\text{O}_3$  and  $\text{La}_{0.6}\text{Ca}_{0.4}\text{Fe}_{0.8}\text{Cu}_{0.2}\text{O}_3$ . As shown in Fig. 1, some structural differences can be distinguished on La-deficient and stoichiometric perovskites mainly related to distinct reflections assigned to CuO. These reflections intensify on  $\text{La}_{0.7}\text{Fe}_{1-y}\text{Cu}_y\text{O}_3$  with a rise in Cu content which reflect extensive copper oxide aggregation. Hence, the stable cell volume irrespective of the Cu content on La-deficient perovskites could be partly explained by copper segregation. Mössbauer spectroscopy also evidence on this series that charge compensation preferentially occurs through the removal of oxygen with related formation of oxygen vacancies. Accordingly, the greater stabilization of  $\text{Fe}^{4+}$  in stoichiometric compositions could reflect a better accommodation of  $\text{Cu}^{2+}$  octahedrally coordinated in the lattice of  $\text{LaFe}_{1-y}\text{Cu}_y\text{O}_3$  whereas  $\text{Fe}^{3+}$  species in different tetrahedral and octahedral symmetries prevail for the series  $\text{La}_{0.7}\text{Fe}_{1-y}\text{Cu}_y\text{O}_3$ . This seems consistent with an easier reduction of segregated CuO extra-framework species observed from  $\text{H}_2$ -TPR experiments compared to  $\text{Cu}^{2+}$  octahedrally coordinated in the perovskite lattice (see Fig. 6). Such an explanation is also consistent with SEM measurements and elemental mapping characterizing CuO clusters on  $\text{La}_{0.7}\text{Fe}_{0.8}\text{Cu}_{0.2}\text{O}_3$ .

A point that emerges from these observations is related to the real implication of these bulk properties in the catalytic performances. In a first attempt, H<sub>2</sub>-TPR and O<sub>2</sub>-TPD experiments can be useful to check if the reducibility and oxygen mobility have an impact on the rate values. O<sub>2</sub>-TPD experiments mostly underline the prevalence of intrafacial O<sub>2</sub> desorption. As exemplified in Figs. S12 and S13, the H<sub>2</sub> uptakes and the amount of oxygen desorbed expressed per gram or m<sup>2</sup> cannot be properly correlated to rate measurements. This emphasizes the fact that neither the reducibility of the B cation nor the bulk oxygen mobility can be considered as critical parameters for explaining the impact of single and dual substitutions on the catalytic properties. The absence of correlation is in agreement with earlier observations provided by Royer et al. [8] who found that changes observed in the reaction rate of methane oxidation on LaCo<sub>1-x</sub>Fe<sub>x</sub>O<sub>3</sub> did not depend on the redox properties, measured by O<sub>2</sub>-TPD and H<sub>2</sub>-TPR. This would a priori suggests a preferential suprafacial mechanism. At first glance, the catalytic properties should therefore be mainly governed by the extent of the catalyst surface. However, the comparison between the rates as well as the pre-exponential factor values of the rate constant with the specific surface do not reveal a clear correlation. Consequently, there is no proportionality between the surface and the density of active sites which seem mostly governed by the extent of copper and calcium substitution appearing as a critical parameters.

Surface composition from semi-quantitative XPS analysis on La<sub>0.7</sub>Fe<sub>1-y</sub>Cu<sub>y</sub>O<sub>3</sub> underlined a gradual increase of copper concentration from  $y = 0.1$  to  $0.3$  which is consistent with copper agglomeration at the surface. On the other hand, such tendency is not discernible on LaFe<sub>1-y</sub>Cu<sub>y</sub>O<sub>3</sub>. The lower B.E. values on the Cu 2p photopeak recorded on La<sub>0.7</sub>Fe<sub>1-y</sub>Cu<sub>y</sub>O<sub>3</sub> and LaFe<sub>1-y</sub>Cu<sub>y</sub>O<sub>3</sub> compared to La<sub>0.7</sub>Ca<sub>x</sub>Fe<sub>1-y</sub>Cu<sub>y</sub>O<sub>3</sub> suggest the formation of oxidic copper in lower valent state. Such species have been assigned to CuO clusters at the surface more reducible than lattice Cu(+II) species. Interestingly, Ca substitution shifts B.E. to higher

values emphasizing the presence of more stable  $\text{Cu}^{2+}$  species in octahedral coordination. Such tendency seems more accentuated on the stoichiometric  $\text{La}_{0.6}\text{Ca}_{0.4}\text{Fe}_{0.8}\text{Cu}_{0.2}\text{O}_3$  exhibiting the lowest surface Cu concentration and the highest abundance of  $\text{Fe}^{4+}$ . Such trends are also consistent with more intense contraction effects on the cell volume observed on the dual-substituted samples notably on  $\text{La}_{0.6}\text{Ca}_{0.4}\text{Fe}_{0.8}\text{Cu}_{0.2}\text{O}_3$ . It is remarkable that Ca-substituted samples become less reducible in comparison with  $\text{La}_{0.7}\text{Fe}_{1-y}\text{Cu}_y\text{O}_3$ . Such an observation could be partly explained by a lesser formation of copper oxide extra-framework species. Nakamura et. al [39] investigated the reducibility of  $\text{La}_{1-x}\text{Sr}_x\text{CoO}_{3-\delta}$ . Interestingly, their observations led them to the conclusion that increasing the perovskites reducibility decreases its ability to refill its oxygen vacancies. Hence, the density, the stability of anionic vacancies and their ability for refilling is expected to be higher on  $\text{La}_{0.6}\text{Ca}_{0.4}\text{Fe}_{0.8}\text{Cu}_{0.2}\text{O}_3$  than on  $\text{La}_{0.7}\text{Fe}_{1-y}\text{Cu}_y\text{O}_3$  and  $\text{LaFe}_{1-y}\text{Cu}_y\text{O}_3$ .



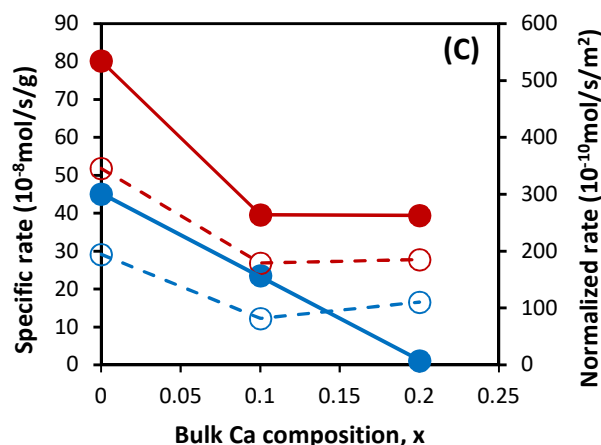


**Fig. 8.** Influence of Ca and Cu substitution on specific, normalized rates and apparent activation energy ( $E_{app}$ ) of stoichiometric and La-deficient perovskite catalysts for CO oxidation – (A)  $\text{LaFe}_{1-y}\text{Cu}_y\text{O}_3$ ; (B)  $\text{La}_{0.7}\text{Fe}_{1-y}\text{Cu}_y\text{O}_3$ ; (C)  $\text{La}_{0.6}\text{Ca}_x\text{Fe}_{1-y}\text{Cu}_y\text{O}_3$  ( $x = 0$  corresponds to  $\text{La}_{0.7}\text{Fe}_{0.8}\text{Cu}_{0.2}\text{O}_3$ ) – STO1 in red and STO2 in blue – Full symbol stands for specific rate and empty symbol stands for normalized rate.

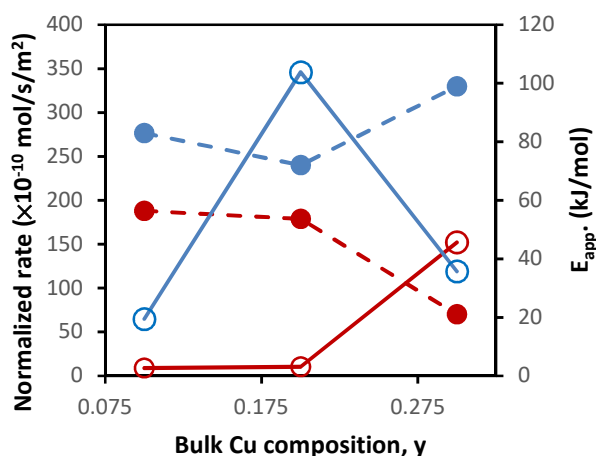


**Fig. 9.** Evolution of the normalized rate and the apparent activation energy ( $E_{app}$ ) from STOI measurements vs bulk copper composition on stoichiometric  $\text{LaFe}_{1-y}\text{Cu}_y\text{O}_3$  (red) and La-deficient  $\text{La}_{0.7}\text{Fe}_{1-y}\text{Cu}_y\text{O}_3$  perovskite catalysts (blue).

Keeping in mind the aforementioned discussion, a closer examination of the role of copper, La-deficiency and calcium substitution come from the examination of Figs. 8 and 9. Interestingly, an optimal Cu composition for  $y = 0.2$  appears in Fig. 8(B) on La-deficient perovskites taking rates calculated from STOI experiments into account. Such an optimum was not originally observed on the stoichiometric samples but appears distinctly from STO2 rate measurements. These evolutions are likely governed by the rate of copper extraction and aggregation at the surface during lean/rich temperature cycles and accentuates with a rise in

copper content. Clearly, these processes would occur much faster on  $\text{La}_{0.7}\text{Fe}_{1-y}\text{Cu}_y\text{O}_3$  than on  $\text{LaFe}_{1-y}\text{Cu}_y\text{O}_3$  and in agreement with the gradual increase of the surface Cu/Fe ratio recorded on  $\text{La}_{0.7}\text{Fe}_{1-y}\text{Cu}_y\text{O}_3$  in Table 5. Subsequent comparisons between rates and apparent activation from STOI1 experiments in Fig. 9 clearly shows that normalized rates for CO oxidation can be explained by the evolution observed on the apparent activation energy. A rise in normalized rate is accompanied to the lessening of  $E_{\text{app}}$ . Hence, the deactivation on  $\text{La}_{0.7}\text{Fe}_{0.7}\text{Cu}_{0.3}\text{O}_3$  corresponding to the highest Cu/Fe ratio and a significant increase in  $E_{\text{app}}$  can be related to a significant agglomeration of less active CuO clusters. This comparison suggests that the evolution on values of  $E_{\text{app}}$  reflects changes in the degree of dispersion and reducibility of extraframework CuO species for the series  $\text{LaFe}_{1-y}\text{Cu}_y\text{O}_3$  and on  $\text{La}_{0.7}\text{Fe}_{1-y}\text{Cu}_y\text{O}_3$ .

Regarding the series  $\text{La}_{0.6}\text{Ca}_x\text{Fe}_{0.8}\text{Cu}_{0.2}\text{O}_3$ , no optimum appears on the rates. A decrease is observed for  $x = 0.1$  then stabilizing at increasing Ca content. Jointly, a decrease in the Cu/Fe ratio is also noticeable but no significant change is observed on  $E_{\text{app}}$ . These observations seem in good agreement with the fact that calcium substitution would partially block copper segregation process avoiding significant agglomeration. All these observations seem to emphasize the role of calcium for monitoring dispersion/agglomeration processes of extraframework CuO. Calcium substitution would protect highly-dispersed CuO species, more reducible than lattice  $\text{Cu}^{2+}$  species, avoiding their coalescence into larger CuO aggregates. Such conclusion seems in reasonable agreement with previous investigations showing that the reduction of  $\text{Cu}^{2+}$  to  $\text{Cu}^+$  is vital for the chemisorption of CO on amorphous CuO highly dispersed on Cu-doped defective perovskite [40]. Jernigan et al. [41] proposed a reaction pathways including the reduction of inactive  $\text{Cu}^{2+}$  to active  $\text{Cu}^+$  by gaseous CO. A mixture of  $\text{Cu}^0$  and  $\text{Cu}^+$  led to rate enhancement in CO oxidation explained by a two-Cu site mechanism that requires two neighbor Cu sites exhibiting two different oxidation states [42].

More recently, Marie et al. [43] concluded that oligomeric Cu species would act as active and selective sites for CO oxidation at low temperature. In case of more complex mixed oxide compositions, optimal performances were observed on mixed Cu and Mn oxide and related to two active sites :  $\text{Cu}^+$  in intimate contact with  $\text{MnO}_x$ , useful for CO oxidation and surface  $\text{Cu}^+$  stabilized in bulky CuO clusters for oxygen refilling [44]. Taking this background into account some analogies with our observations can be established which agree with a conventional suprafacial mechanism by considering the superiority of active  $\text{Cu}^+$  species from the partial reduction of CuO to activate CO, while neighbor surface anionic species would ease  $\text{O}_2$  adsorption. Copper agglomeration would destabilize this compromise then explaining the lower activity recorded on  $\text{La}_{0.7}\text{Fe}_{0.7}\text{Cu}_{0.3}\text{O}_3$  for CO conversion.

Quite similar tendencies reproduce for propene oxidation but in lower extent with an optimum observed on  $\text{La}_{0.7}\text{Fe}_{1-y}\text{Cu}_y\text{O}_3$  still prevailing from STO2 reaction rates (see Fig. 10). A rate enhancement also appears at increasing copper content on  $\text{La}_{0.7}\text{Fe}_{1-y}\text{Cu}_y\text{O}_3$ . In contrast, no relevant comparison can be drawn from the normalized rates and the apparent activation energy especially for the series  $\text{La}_{0.7}\text{Fe}_{1-y}\text{Cu}_y\text{O}_3$ . Regarding the impact of calcium, sharp differences appear on the evolution of the specific and normalized rates. In contrary to the slight detrimental effect noticeable for CO oxidation due to calcium substitution, an opposite beneficial effect can be observed. Previously, a significant rate enhancement was associated with a rise in calcium content. Merino et al. [31] who substituted  $\text{La}^{3+}$  by  $\text{Ca}^{2+}$  into  $\text{LaCoO}_3$  lattice also observed distinctly an increase in superficial oxygen vacancy densities yielding promoted catalytic activities for propane oxidation. Nevertheless, this effect is noticeable mostly on La-deficient sample as reported in Fig. 10(C). Surprisingly a sharp loss of activity is observable on  $\text{La}_{0.6}\text{Ca}_{0.4}\text{Fe}_{0.8}\text{Cu}_{0.2}\text{O}_3$  during STO1 and STO2 cycles which manifests a detrimental effect of calcium accompanied with a significant increase in the apparent activation energy. As previously argued, the comparison of  $\text{O}_2$ -TPD profile could partly

explain such change in kinetic behavior. It is remarkable that dual substitution on La-deficient materials delay the  $\beta$ -oxygen desorption which agrees with a preferential suprafacial mechanism. On the other hand,  $\beta$ -oxygen desorption occurs more readily on  $\text{La}_{0.6}\text{Ca}_{0.4}\text{Fe}_{0.8}\text{Cu}_{0.2}\text{O}_3$  and is also accompanied with a more intense suprafacial oxygen desorption below  $400^\circ\text{C}$ . Such observation seems to agree with previous explanations emphasizing the fact that an oxygen depletion of the surface takes place with a rise in temperature and could be replenished at high temperature thanks to bulk diffusion insuring a gradual transition to the intrafacial mechanism on  $\text{La}_{0.6}\text{Ca}_{0.4}\text{Fe}_{0.8}\text{Cu}_{0.2}\text{O}_3$ . Accordingly the  $\text{Fe}^{4+}/\text{Fe}^{3+}$  redox couple could be also involved in propene oxidation. In practice, more probably a mixed kinetic regimes would occur as aforementioned. Such an explanation seems to be consistent with previous discussions on the bulk reducibility of perovskites in agreement with the observations provided by Nakamura et al. [39] suggesting that the density, the stability of anionic vacancies and their ability for refilling is expected to be higher on  $\text{La}_{0.6}\text{Ca}_{0.4}\text{Fe}_{0.8}\text{Cu}_{0.2}\text{O}_3$  than on  $\text{La}_{0.7}\text{Fe}_{1-y}\text{Cu}_y\text{O}_3$  and  $\text{LaFe}_{1-y}\text{Cu}_y\text{O}_3$ .

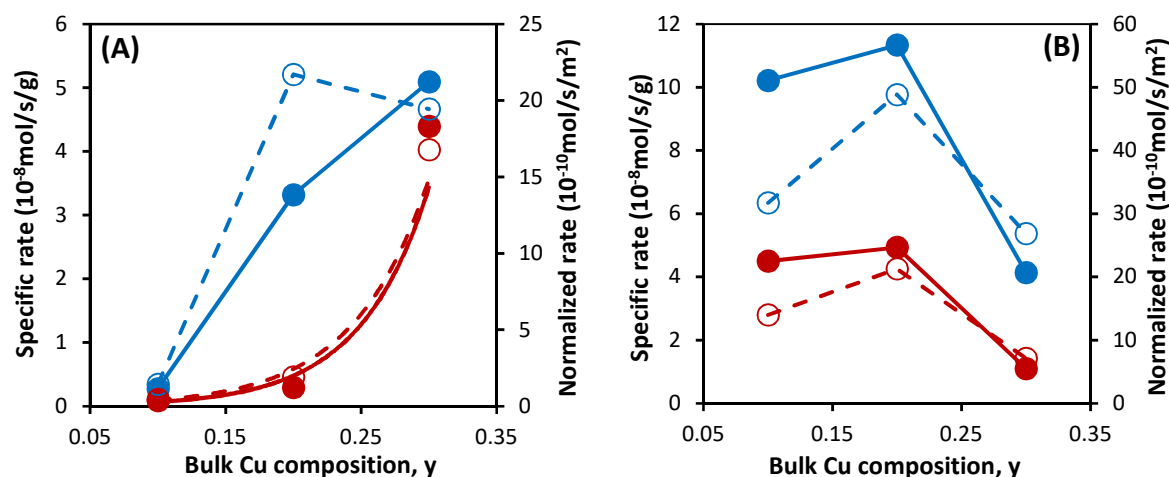
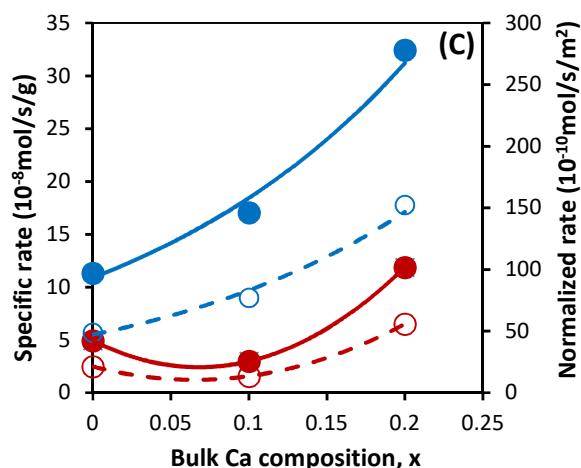


**Fig. 10.** Influence of Ca and Cu substitution on specific and normalized rates of stoichiometric and La-deficient perovskite catalysts for propene oxidation – (A)  $\text{LaFe}_{1-y}\text{Cu}_y\text{O}_3$ ; (B)  $\text{La}_{0.7}\text{Fe}_{1-y}\text{Cu}_y\text{O}_3$ ; (C)  $\text{La}_{0.6}\text{Ca}_x\text{Fe}_{1-y}\text{Cu}_y\text{O}_3$  ( $x = 0$  corresponds to  $\text{La}_{0.7}\text{Fe}_{0.8}\text{Cu}_{0.2}\text{O}_3$ ) –STO1 in red and STO2 in blue – Full symbol stands for specific rate and empty symbol stands for normalized rate.



## 5. Conclusion

Single and dual substitutions of parent stoichiometric  $\text{LaFeO}_3$  and La-deficient  $\text{La}_{0.7}\text{FeO}_3$  have been investigated for CO and propene oxidation in typical three-way conditions. Calcium and copper doping in A-site and B-site respectively has been implemented with the aim to modulate the oxidation state of B-site and the oxygen mobility through structural distortions. It was found that the resulting features differ from according to stoichiometric and La-deficient perovskite compositions. Two mechanisms of charge compensation are proposed in response to substitution of La by Ca in A-site and Fe by Cu in B-site associated to the generation of anionic vacancies causing disorder of crystal structure and the stabilization of  $\text{Fe}^{4+}$  in B-site. Mössbauer spectroscopy characterized the presence of  $\text{Fe}^{4+}$  cations only on stoichiometric compositions related to a better accommodation of  $\text{Cu}^{2+}$  in the crystal structure whereas, copper segregation and agglomeration processes occur much faster on La-deficient perovskites. Well-dispersed extra-framework copper species lead to a significant rate enhancement likely related to a partial reduction of  $\text{Cu}^{2+}$  to more active  $\text{Cu}^+$  associated to surface anionic vacancies able to adsorbed gaseous oxygen. On the other hand, a rise in copper content as well as successive lean/rich exposure can speed up segregation process then leading to larger CuO aggregates less active in CO and propene oxidation. For  $\text{La}_{0.7}\text{Fe}_{1-y}$

$y\text{Cu}_y\text{O}_3$ , an optimum Cu-doping of  $y = 0.2$  is associated with the highest specific and normalized reaction rate both for CO and  $\text{C}_3\text{H}_6$  oxidation. Dual substitution showed that Cu segregation is partly inhibited then minimizing the density of accessible active copper species. As a consequence, a slight detrimental effect is observed on the rate of CO oxidation but no deactivation appears due to CuO aggregation. On the contrary, a beneficial effect manifests in propene oxidation on A-deficient compositions, emphasizing the fact that copper would play a minor role on this series. Interestingly, the opposite trend is observed on  $\text{La}_{0.6}\text{Ca}_{0.4}\text{Fe}_{0.8}\text{Cu}_{0.2}\text{O}_3$  with a sharp loss in propene oxidation. This observation has been interpreted based on a progressive shift from suprafacial to intrafacial mechanism on  $\text{La}_{0.6}\text{Ca}_x\text{Fe}_{0.8}\text{Cu}_{0.2}\text{O}_3$  (with  $x = 0.1$  or  $0.2$ ) involving the redox  $\text{Fe}^{4+}/\text{Fe}^{3+}$  couple in the course of the reaction.

## Acknowledgements

The authors acknowledge financial support by the EU-Partial-PGMs project (H2020-NMP-686086). Chevreul Institute (FR 2638), Ministère de l'Enseignement Supérieur et de la Recherche, Région Nord – Pas de Calais and FEDER are acknowledged for supporting and funding partially this work. We also thank Martine Trentesaux and Pardis Simon who conducted XPS measurements and Olivier Gardoll for thermal analysis.

## Reference

1. S.C. Sorenson, J.A. Wronkiewicz, L.B. Sis, G.P. Wirtz, American Ceramic Society Bulletin 53 (1974) 446-449.
2. C.H. Kim, G. Qi, K. Dahlberg, W. Li, Science 327 (2010) 1624-1627.
3. J. Zhu, A. Thomas, Appl. Catal. B 92 (2009) 225-233.
4. H. He, H.X. Dai, C.T. Au, Appl. Catal. B 33 (2011) 65-80.
5. A. Glisenti, M. Pacella, M. Guitto, M.M. Natile, P. Canu, Appl. Catal. B 180 (2016) 94-105.
6. M. Pacella, A. Garbujo, J. Fabro, M. Guitto, Q. Xin, M.M. Natile, P. Canu, P. Cool, A. Glisenti, Appl. Catal. B 227 (2018) 446-458.
7. R. Zhang, A. Villanueva, H. Alamdari, S. Kaliaguine, Appl. Catal. B 64 (2006) 220-233.
8. R. Zhang, A. Villanueva, H. Alamdari, S. Kaliaguine, Appl. Catal. A 307 (2006) 85-97.
9. K. Simmance, D. Thompsett, W. Wang, B. Thiebaut, Catal. Today, 320 (2019) 40-50.

10. Y. Nishihata, J. Mizuki, T. Akao, H. Tanaka, M. Uenishi, K. Kimura, T. Okamoto, N. Hamada, *Nature* 418 (2002) 164-167.
11. M. Uenishi, M. Taniguchi, H. Tanaka, M. Kimura, Y. Nishihata, J. Mizuki, T. Kobayashi, *Appl. Catal. B* 57 (2005) 267-273.
12. I. Rosetti, O. Buchneva, C. Biffi, R. Rizza, *Appl. Catal. B* 89 (2009) 383-390.
13. Y. Zhang-Steenwinkel, H.L. Castricum, J. Bekers, E. Eiser, A. Bliet, *J. Catal.* 221 (2004) 523-531.
14. P. Granger *Catal. Sci. Technol.* 7 (2018) 5195-5211.
15. C. Morgan, Johnson Matthey *Technol. Rev.* 59 (2015) 188-192.
16. S. Li, R. Kato, Q. Wang, T. Yamanaka, T. Takeguchi, W. Ueda, *Appl. Catal. B* 93 (2010) 383-386.
17. F. Fang, N. Feng, L. Wang, J. Meng, G. Liu, P. Zhao, P. Gao, J. Ding, H. Wan, G. Guan, *Appl. Catal. B* 236 (2018) 184-194.
18. A. Schön, C. Dujardin, J.P. Dacquin, P. Granger, *Catal. Today*, 258 (2015) 543-548.
19. J. Emmerlich, B.M. Linke, D. Music, J.M. Schneider, *Solid State Ionics* 255 (2014) 108-112
20. R. Pushpa, D. Daniel, D.P. Butt, *Solid. State Ionics*, 249-250 (2013) 184-190.
21. S.D. Peter, E. Garbowski, V. Perrichon, B. Pommier, M. Primet, *Appl. Catal. A* 205 (2001) 147-158.
22. H. Taguchi, S. Matsu-ura, M. Nagao. *J. Solid State Chem.* 129 (1997) 60-65.
23. T. Caronna, F. Fontana, I. Natali Sora, R. Pelosato *Mater. Chem. Phys.* 116 (2009) 645-648.
24. Y. Wu, T. Yu, B. Dou, C. Wang, X. Xie, Z. Yu, S. Fan, L. Wang. *J. Catal.* 120 (1989) 88-107.
25. B.P. Barbero, J. Andrade Gamboa, L.E. Cadus. *Appl. Catal. B* 65 (2006) 21-30.
26. U. Russo L. Nodari, M. Faticanti, V. Kuncser, G. Filoti, *Solid State Ionic* 176 (2005) 97-102.
27. P.D. Battle, T.C. Gibb, S. Nixon, *J. Solid State Chem.* 79 (1989) 75-85.
28. L.G. Tejuca, J.L.G. Fierro, J.M.D. Tascón, *Adv. Catal.* 36 (1989) 237-328.
29. B. Lévassieur, S. Kaliaguine, *Appl. Catal. B* 88 (2009) 305-314.
30. Y. Wu, L. Li, B. Bhu, Y. Li, Z. Qin, M. Fan, Q. Qin, H. He, L. Zhang, L. Dong, B. Li, L. Dong, *Appl. Catal. A* 568 (2018) 43-53.
31. N.A. Merino, B.P. Barbaro, P. Grange, L.E. Cadús, *J. Catal.* 231 (2005) 232-244.
32. F.E. Lopez-Suarez, S. Parres-Esclapez, A. Bueno-López, M.J. Illán-Gómez, B. Ura, J. Trawczynski *Appl. Catal. B* 93 (2009) 82-89.
33. L. Zhang, Y. Nie, C. Hu, J. Qu. *Appl. Catal. B* 125 (2012) 418-424.
34. T. Yano, M. Ebizuka, S. Shibata, M. Yamane *J. Electron Spectrosc. Relat. Phenom.* 131-132 (2003) 133-144.
35. A. Schön A, J.P. Dacquin, P. Granger, C. Dujardin, *Appl. Catal. B* 223 (2018) 167-176.
36. F. Amano, T. Tanaka, T. Funabiki. *J. Mol. Catal. A* 221 (2004) 89-95.
37. J.L. Hueso, D. Martínez-Martínez, A. Caballero, A.R. González-Elípe, B.S. Mun, M. Salmerón *Catal. Comm.* 10 (2009) 1898-1902.
38. R.J.H. Voorhoeve, in: J.J. Burton, R.L. Garten (Eds.), *Advanced Materials in Catalysis*, Academic Press, New York, 1977, p. 129.
39. T. Nakamura, M. Misono, Y. Yoneda, *J. Catal.* 83 (1983) 151-159.
40. Y. Yi, H. Liu, B. Chu, Z. Qin, L. Dong, H. He, C. tang, M. Fan, L. Bin, *Chem. Eng. J.* 369 (2019) 511-521.
41. G.G. Jernigan, G.A. Somorjai, *J. Catal.* 147 (1994) 567-577.
42. G.J. Wu, N.J. Guan, L.D. Li, *Catal. Sci. Technol.* 1 (2011) 601-608.
43. O. Marie, X. Portier, N. Korsunska, L. Khomenkova *Appl. Catal.* (2020) 119258.
44. A. Davó-Quñoneroa, I. Such-Basáñezc, J. Juan-Juan, D. Lozano-Castelló, P. Stelmachowski, G. Grzybek, A. Kotarba, A. Bueno-López *Appl. Catal. B* 267 (2020) 118372.

# Graphical Abstract

